DESIGN, FABRICATION AND CHARACTERIZATION OF III-NITRIDE PN JUNCTION DEVICES

A Thesis
Presented to
The Academic Faculty

by

Jae Boum Limb

In Partial Fulfillment
of the Requirements for the Degree
Doctor of Philosophy in the
School of Electrical and Computer Engineering

Georgia Institute of Technology
August 2007

DESIGN, FABRICATION AND CHARACTERIZATION OF III-NITRIDE PN JUNCTION DEVICES

Approved by:

Dr. Russell Dupuis, Advisor
School of Electrical and Computer Engineering
Georgia Institute of Technology

Dr. Joy Laskar
School of Electrical and Computer Engineering
Georgia Institute of Technology

Dr. William Doolittle
School of Electrical and Computer Engineering
Georgia Institute of Technology

Dr. David Citrin
School of Electrical and Computer Engineering
Georgia Institute of Technology

Dr. Srinivas Garimella
School of Mechanical Engineering
Georgia Institute of Technology

Date Approved: June 26, 2007

ACKNOWLEDGEMENTS

I would like to express my sincere gratitude to those who have helped make this work possible. First, I would like to thank my supervising advisor, Professor Russell Dean Dupuis, for his guidance and for giving me the opportunity to work in his group. His depth of understanding and ability to relate many ideas together has provided the push in the right direction and has made this work possible. I would also like to thank Professor Shyh-Chiang Shen for letting me use his lab, Professor Alan Doolittle for useful comments on device analysis and Professor David Citrin for kindly serving on my reading committee. I would also like to thank Professors Joy Laskar and Srinivas Garimella for serving on my committee as well.

I would like to extend my heartfelt thanks to my colleagues in the AMDG group: Dr. Jae-Hyun Ryou, Dr. Peng Li, Dr. Uttiya Chowdhury, Dr. Theodore Chung, Dr. Jianping Liu and Dr. Xuebing Zhang for their cooperation, their help, and for all the informative discussions we had together. I would especially like to thank Dongwon Yoo and Wonseok Lee for their friendship and for providing me with good materials, Andy Ewing for his ability to explain and discuss complex topics with me, Yong Huang for his challenging discussions on materials issues, Yair Korenblit for helpful comments, Clarissa Grayson for taking over my projects, Leslie Schlag for a fantastic job at administrative stuff, and all the other people who I have unintentionally left out.

I would also like to acknowledge the help of those outside my research group who provided assistance in many ways. Specific thanks go to Dr. Meredith Reed and Dr. Chuck Collins of Army Research Labs for help with UV detection measurements and Dr. Jeongsoo Park of Epivalley for useful ideas on Green LED structures. I also thank those in Dr. Shen's group, especially Yun Zhang for his help with spectral response measurements.

The staff at the Microelectronics Research Center has been helpful and a pleasure to work with. Special thanks go to Gary Spinner, Tran-Vinh Nguyen and Charlie Suh for their hard work on equipment maintenance. None of this work would have been possible without their assistance.

Finally, I consider myself extremely fortunate to have wonderful parents who have always set a strong example for me and have supported me through all of the accomplishments of my academic life. I also owe much to my wife Yoon Soo Park, who has always inspired me to be at my very best and to realize my full potential.

TABLE OF CONTENTS

Page

ACKNOWLEDGEMENTS iv

LIST OF TABLES ix

LIST OF FIGURES x

SUMMARY xiv

CHAPTER

1 INTRODUCTION………………………………………………………………. 1

1.1 Group III Nitride Semiconductor Structure and Characteristics…………1

1.2 Motivation for III-Nitride Photodetectors………………………………..4

1.3 Motivation for III-Nitride Devices in Visible Optoelectronics…………..5

1.4 Motivation for III-Nitride Devices in Power Electronics………………...8

1.5 Scope of this Dissertation………………………………………………10

2 CHARACTERIZATION TECHNIQUES……………………………………....12

2.1 Material Characterizations……………………………………………....12

2.1.1 X-ray Diffraction…………………………………………………12

2.1.2 Photoluminescence and Cathodoluminescence…………………...13

2.1.3 Transmission Electron Microscopy……………………………… 16

2.2 Surface Characterizations…………………………………………… 17

2.2.1 Atomic Force Microscopy……………………………………….. 17

2.2.2 Scanning Electron Microscopy…………………………………... 18

2.2.3 Secondary Ion Mass Spectroscopy………………………………. 18

2.3 Electrical Characterizations……………………………………………. 19

2.3.1 Hall Effect……………………………………………………….... 19

2.3.2 Transmission Line Measurements………………………………….. 20

2.3.3 DC Current-Voltage Measurements………………………………22

2.3.4 Electroluminescence…………………………………………….... 22

3 OPERATING PRINCIPLES OF RELEVANT DEVICES……………………. 24

3.1 Introduction…………………………………………………………..24

3.2 PIN Photodetectors………………………………………………….. 24

3.3 Light-Emitting Diode Basics………………………………………... 27

3.3.1 Injection Luminescence and Radiative Recombination…………..27

3.3.2 External Quantum Efficiency……………………………………..29

3.3.3 Emission Spectrum………………………………………………. 29

3.3.4 Heterostructures………………………………………………….. 30

3.4 PIN Rectifiers………………………………………………………...30

3.4.1 Forward Conductivity Modulation………………………………..32

4 III-NITRIDE AVALANCHE PHOTODIODES………………………………. 34

4.1 Introduction………………………………………………………….34

4.2 GaN Avalanche Photodiodes…………………………………………...35

4.3 Dielectric Effects on the Performance of Avalanche Photodiodes……..39

4.4 $Al_{0.05}Ga_{0.95}N$ Avalanche Photodiodes………………………………..42

4.5 Summary…………………………………………………………….. 48

5 III-NITRIDE GREEN LIGHT EMITTING DIODES…………………......... 49

5.1 Introduction…………………………………………………………..49

5.2 Motivation for Using *p*-InGaN………………………………………….50

5.3 Comparison of LEDs Using *p*-InGaN and *p*-GaN Emitting at ~518 nm..52

5.4 Effect of Silicon doping of Quantum Well Barriers on LED Performance……………………………………………………………..60

5.5 Green LEDs Emitting at 525nm and Longer Wavelengths……………..62

5.6 Summary………………………………………………………………….. 67

6 III-NITRIDE PIN RECTIFIERS…………………………………………….68

6.1 III-Nitride *p-i-n* Rectifiers as Power Devices…………………………...68

6.2 Vertical Mesa Rectifier Structure on SiC Substrate…………………….68

6.2.1 Vertical Mesa *p-i-n* Rectifiers on SiC Substrates……………...69

6.3 Vertical Mesa *p-i-n* Rectifiers on Freestanding GaN Substrates……….72

6.4 Rectifier Structure on SiC Substrate Using a Conducting Buffer Layer.75

6.4.1 Full-Vertical *p-i-n* Rectifiers…………………………………..77

6.5 Summary………………………………………………………………….. 82

7 RESEARCH SUMMARY AND FUTURE WORK……………………………83

7.1 Avalanche Photodiodes……………………………………………....83

7.2 Green Light Emitting Diodes……………………………………...85

7.3 PIN Rectifiers……………………………………………………...88

REFERENCES……………………………………………………………………….89

VITA…………………………………………………………………………………94

LIST OF TABLES

Page

Table 1.1: Si, GaAs, 4H-SiC, 6H-SiC, and GaN material properties……………………. 9

Table 4.1: Composition, doping, and thickness of the layers of a GaN APD…………..35

LIST OF FIGURES

Page

Figure 1.1: Diagram of the wurtzite structure for group III-nitride materials……………2

Figure 1.2: Bandgap versus a-lattice constant for the $In_xAl_yGa_{1-x-y}N$ system…………....3

Figure 1.3: Energy gap vs lattice constant of III-V semiconductor materials for visible light emitting device applications……………………………………………..6

Figure 2.1: Plain view of the TLM pattern showing the semiconductor mesa with dark metal pad…………………………………………………………………..21

Figure 2.2: Plot of measured resistance versus contact spacing………………………...21

Figure 3.1: Schematic band diagram of an electroluminescent *p-n* junction under a forward bias condition………………………………………………………28

Figure 3.2: Comparison of punch-through diode structure with normal *p-n* junction diode…………………………………………………………………….31

Figure 4.1: SEM image of a fabricated 30μm-diameter GaN APD device……………..36

Figure 4.2: Reverse-bias dark-current characteristics of a GaN APD having a circular mesa of 30 μm diameter, showing a low dark current and current density of 2×10^{-11} A and 3.5×10^{-6} A/cm^2 respectively, just before avalanche breakdown…………………………………………………………….....37

Figure 4.3: Reverse-bias *I-V* characteristics of a GaN APD having a mesa diameter of 50 μm. The dark current, photocurrent, and avalanche gain (M) are plotted versus reverse bias voltage. The diode shows gain in excess of M~10 at the onset of avalanche breakdown (-86.5V, electric field of ~2.8 MV/cm), reaching a maximum avalanche gain greater than ~3,000…..……………….38

Figure 4.4: Dark current comparisons for APDs with SiO_2 and SiN passivations. The devices had a mesa diameter of 30 μm…………………………………....41

Figure 4.5: Photocurrent comparisons for APDs with SiO_2 and SiN passivations. The devices had a mesa diameter of 30 μm………………………………………42

Figure 4.6: Schematic diagram of the $Al_{0.05}Ga_{0.95}N$ APD mesa-geometry device structure grown on a bulk GaN substrate……………………………………44

Figure 4.7: AFM microscopic surface morphology of an $Al_{0.05}Ga_{0.95}N$ ultraviolet APD wafer grown on a bulk GaN substrate: (a) 5×5 μm^2 scan (b) 1×1 μm^2 scan with a z-height scale of 10 nm…………………………………......................45

Figure 4.8: Reverse-bias *I-V* characteristics of an $Al_{0.05}Ga_{0.95}N$ ultraviolet avalanche photodiode having a mesa diameter of 30 µm. The illumination is provided by a ~250 nm source. The dark current, photocurrent, and avalanche gain are plotted versus reverse bias voltage. The diode exhibits a maximum avalanche gain ~50 at a reverse bias of 86.75V…………………………...46

Figure 4.9: Spectral response for $Al_{0.05}Ga_{0.95}N$ ultraviolet avalanche photodiode having a mesa diameter of 30 µm. The voltage was varied from 0 to -80 V. The photocurrent starts to show significant increases from -60 Volt bias………..47

Figure 5.1: Influence of *p*-GaN and *p*-InGaN layer on the optical properties of green LED. (1) Without a *p*-layer, (2) With a *p*-InGaN layer grown at 840° C, (3) With a *p*-GaN layer grown at 930° C……………………………………...51

Figure 5.2: TLM *I-V* comparisons for LEDs with different *p*-layers…………………...52

Figure 5.3:SEM Images of green LEDs: (a) 230µm and 350µm, and (b) 1mm Devices.54

Figure 5.4: Schematic structures of the green LEDs in this study with (a) *p*-$In_{0.04}Ga_{0.96}N$: Mg grown at 840°C, and (b) *p*-GaN:Mg layer grown at 930°C…………….55

Figure 5.5: The room temperature EL spectra of green LEDs at low current levels: (a) with *p*-$In_{0.04}Ga_{0.96}N$:Mg layer; (b) with *p*-GaN:Mg layer. Note that the EL peak changes significantly for LED with *p*-$In_{0.04}Ga_{0.96}N$:Mg layer at all current levels, while virtually no change is shown for LED with *p*-GaN:Mg layer………………………………………………………………………. 55

Figure 5.6: The room temperature EL spectra of green LEDs at high current levels: (a) with *p*-$In_{0.04}Ga_{0.96}N$:Mg layer; (b) with *p*-GaN:Mg layer. Note that the EL peak does not change much once the current level exceeds 20 mA for both cases……………………………………………………………………….57

Figure 5.7: Current-voltage characteristics of green LEDs with different *p*-layers at room temperature. The LED with *p*-$In_{0.04}Ga_{0.96}N$ layer show slightly higher V_f of ~3.2 V at 20 mA, while LED with *p*-GaN layer show a V_f of ~3.1 V. However, the LED with *p*-$In_{0.04}Ga_{0.96}N$ layer clearly shows lower diode series resistance……………………………………………………………58

Figure 5.8: Simulated band-diagram of LEDs with *p*-$In_{0.04}Ga_{0.96}N$ and *p*-GaN layers drawn together: *p*-layers, UID GaN barrier, and first QW are drawn. For LED with a *p*-$In_{0.04}Ga_{0.96}N$ layer, there is an abrupt heterojunction barrier between the *p*-$In_{0.04}Ga_{0.96}N$ and UID GaN layers…………………………....59

Figure 5.9: Current-voltage characteristics of green LEDs with different Si-doping in the QWB. The Si doping was varied from Si = 0 sccm, Si = 4 sccm, and Si = 8 sccm in GaN QWB. V_f =3.85 V, 3.65 V, and 3.48 V at 20 mA, for Si = 0 sccm, 4 sccm, and 8 sccm respectively……………………………….61

Figure 5.10: Electroluminescence characteristics of the green LEDs having different Si doping level in GaN QWB: (a) Si = 0 sccm (unintentionally doped), (b) Si = 4 sccm, and (c) Si = 8 sccm……………………………………………………61

Figure 5.11: The structure for green LEDs emitting at ~526 nm……………………….63

Figure 5.12: (a) EL characteristics of green LEDs emitting at 526 nm at 20 mA (b) *I-V* characteristics of the diode showing a forward voltage of 3.66V at 20 mA... 63

Figure 5.13: The structure for green LEDs emitting at ~545 nm……………………….64

Figure 5.14: (a) EL characteristics of green LEDs emitting at 545 nm at 20 mA (b) *I-V* characteristics of the diode showing a forward voltage of 3.58 V at 20 mA.. 64

Figure 5.15: Simulated band-diagram of an LED emitting at green and longer wavelengths, using a *p*-$In_{0.04}Ga_{0.96}N$ layer and an active region with an indium composition of 30% in the QWs...…………………………………..65

Figure 5.16: Transparent *p*-contact characteristics of an LED emitting at green and longer wavelengths, with a *p*-$In_{0.04}Ga_{0.96}N$ layer. Ni/Au = 5nm/5nm was annealed at 600 ^{o}C in an oxygen ambient to achieve linear contact characteristics…………………………………………………………..66

Figure 6.1: A schematic diagram of the *p-i-n* GaN rectifier structure…………………69

Figure 6.2: SEM image of the fabricated device with mesa dimension of 80 um……... 70

Figure 6.3: Current-voltage characteristics of a mesa etched GaN *p-i-n* rectifier in log-scale………………………………………………………………………. 71

Figure 6.4: Forward current-voltage characteristics of a mesa etched GaN *p-i-n* rectifier……………………………………………………………………….71

Figure 6.5: A schematic epitaxial layer and device structure…………………………...72

Figure 6.6: SEM image of the *p-i-n* GaN rectifier with a mesa diameter of 80 µm employed in this work……………………………………………………..73

Figure 6.7: Semi-logarithmic plot of the current density versus voltage measured for a typical GaN *p-i-n* rectifier with a mesa diameter of 80 µm…………………73

Figure 6.8: Forward *I-V* characteristics for the device with a mesa diameter of 80 µm, in linear-scale………………………………………………………………...74

Figure 6.9: Forward *I-V* characteristics for the device with a mesa diameter of 80 µm, in log-scale…………………………………………………………………….. 75

Figure 6.10: The vertical transport characteristics of $Al_{0.1}Ga_{0.9}N$:Si conducting buffer layer grown on an *n*-type 6H-SiC substrate……………………………… 78

Figure 6.11: (a) Schematic structure of a full-vertical GaN *p*-*i*-*n* rectifier used in this work and (b) energy band diagram of the epitaxial structure in thermal equilibrium: (i) *p*-GaN:Mg, (ii) unintentionally doped *i*-GaN, (iii) *n*-GaN:Si, (iv) AlGaN-GaN grading, (v) AlGaN conducting buffer layer , and (vi) *n*-SiC substrate…………………………………………………………… 80

Figure 6.12: A full-vertical GaN *p*-*i*-*n* rectifier (a) without a current guiding isolation in the *p*-layer (b) with a current guiding isolation in the *p*-layer..……..……… 80

Figure 6.13: (a) Current-voltage characteristics of a full-vertical GaN *p*-*i*-*n* rectifier (log-scale) (b) Current-voltage characteristics of a full-vertical *p*-*i*-*n* rectifier (linear-scale)……………………………………………………………81

Figure 7.1: Vanadium/Aluminum/Titanium/Gold *n*-contact *I*-*V* characteristics of an *n*-type $A_{0.52}G_{0.48}aN$ layer with different contact spacings. Specific contact resistivity was measured and calculated to be $4.15\times10^{-5}\ \Omega\cdot cm^2$. Metal was annealed at 750 ^{o}C in Nitrogen ambient……………………………………..84

Figure 7.2: Comparison of reverse leakage *I*-*V* characteristics between an LED employing *p*-InGaN super-lattice, and an LED with a *p*-InGaN layer……...87

Figure 7.3: Transparent Ni/Au *p*-contact characteristics of Green LEDs with different *p*-layers: (a) *p*-TLM on LED with *p*-InGaN super-lattice (b) *p*-TLM on LED with *p*-InGaN layer…………………………………………………………87

SUMMARY

This dissertation describes an investigation of three types of III-nitride (AlInGaN) based *p-n* junction devices that were grown by metalorganic chemical vapor deposition (MOCVD). The three types of devices are Ultra-Violet (UV) avalanche photodiodes (APDs), green light emitting diodes (LEDs), and *p-i-n* rectifiers.

For avalanche photodiodes, the objective of research was to develop devices that operate in avalanche mode, with high optical gains under UV illumination. High defect density of the material and immature processing technology has hampered the development of III-nitride APDs in the past. To solve this problem, we propose material growth on low-dislocation density GaN substrates, processed with low-damage etching receipes and high quality dielectric passivations. Using this technology, GaN APDs with optical gains greater than 3000 have been demonstrated and AlGaN APDs showing true avalanche gains have also been demonstrated.

For green LEDs, we propose the use of InGaN:Mg as the *p*-layer, rather than employing the conventional GaN:Mg. Not only is InGaN:Mg an active region friendly *p*-layer, but also exhibits higher hole concentrations compared to GaN:Mg. We have shown that green LEDs employing *p*-InGaN exhibit higher emission intensities and lower diode series resistances compared to LEDs with *p*-GaN. Using *p*-InGaN layers, LEDs emitting at green and longer wavelengths have been realized.

For *p-i-n* rectifiers, we have grown, fabricated and characterized devices using the conventional mesa-etch configuration, as well as the full-vertical method. The conventional method requires a low-damage etching technique as well as a high-quality

dielectric passivation. The full-vertical rectifiers avoid the deep-etching of the mesa and field-crowding at the bottom of the mesa. We have taken both approaches to improve the device performances.

In this report, three different types of Nitride based *p-n* junction devices have been grown, fabricated, and characterized. The new approaches in this thesis should enable improved *p-n* junction devices for III-nitride based materials.

CHAPTER 1

INTRODUCTION

Unlike semiconductors based on silicon (Si) and gallium arsenide (GaAs), III-nitride materials are well suited for devices operating at high temperatures and in hostile environments. They are also well suited for emitters or detectors for wavelengths shorter than λ = ~400 nm. Group III nitride materials, including gallium nitride (GaN), aluminum nitride (AlN), and indium nitride (InN), have evoked interest because of their wide applicability to optoelectronic devices. By alloying with AlN and InN, GaN-based material systems can cover a wide range of wavelengths, from red to ultraviolet (650 nm to 200 nm), for light emitting diodes (LEDs) and avalanche photodiodes (APDs). Because of the high electron drift velocity, wide bandgap, and high thermal conductivity, GaN-based electronic devices are promising not only as high-speed devices, but also as high-voltage and high-temperature devices suitable for functioning in chemically hostile environments. While taking advantage of their unique material properties, research has been conducted on three types of III-nitride *p-n* junction devices: APDs, green LEDs, and *p-i-n* rectifiers.

1.1 Group III-Nitride Semiconductor Structure and Characteristics

Group III-nitride semiconductors exist in both cubic (zinc-blende) and hexagonal (wurtzite) crystalline forms. However, the wurtzite phase is the dominant meta-stable state at low pressures. The wurtzite structure of group III-nitride material has a

hexagonal unit cell with two lattice constants, a, and *c*. The unit cell contains six nitrogen atoms and six atoms from the column III of the periodic table of the elements. The volume occupied by these twelve atoms is related to the lattice constants a, and c by equation 1. As displayed in Figure 1.1, the wurtzite structure consists of two interpenetrating hexagonal close-packed sub-lattices, each with one type of atom, offset along the c-axis by 3/8 of the cell height. The space grouping for such a wurtzite structure is $P6_3mc$ or C_{6v}^4.

$$V = 3 \cdot \frac{\sqrt{3}}{2} \cdot a^2 \cdot c \tag{1.1}$$

One of the key properties of the Group III-nitride semiconductors comes from the fact that the wurtzite form of any $In_xAl_yGa_{1-x-y}N$ alloy has a large and direct bandgap. Figure 1.2 represents the bandgap versus the "*a*" lattice parameter for the binary alloys GaN, InN, AlN symbolized by the stars, the ternary alloys $Al_xGa_{1-x}N$, InGaN, InAlN symbolized by the solid lines, and the quaternary alloys InAlGaN existing only in the closed triangular-shaped area.

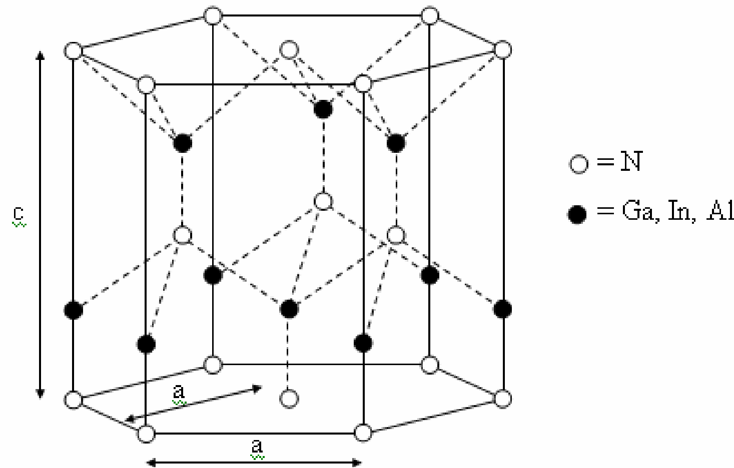

Figure 1.1: Diagram of the wurtzite structure for group III-nitride materials

The lattice constant of the main substrates of choice for the growth of Group III-nitride semiconductors is indicated by the straight vertical lines. Obviously neither silicon carbide (6H-SiC) nor sapphire (Al_2O_3), to a much greater extent, can fulfill the need for lattice-matched substrate required for the epitaxial growth of nitride-based material. However, a relatively high-quality material can still be grown on both SiC and sapphire with the help of a buffer layer. Of course, the quality of an epitaxially grown nitride-based material could be greatly improved with the existence of the bulk GaN substrates, which is lattice matched to the Group III-nitride epitaxial layers. With the recent introduction of bulk GaN substrates, it is hopeful that these lattice matched substrates will provide reduced defect densities of the material.

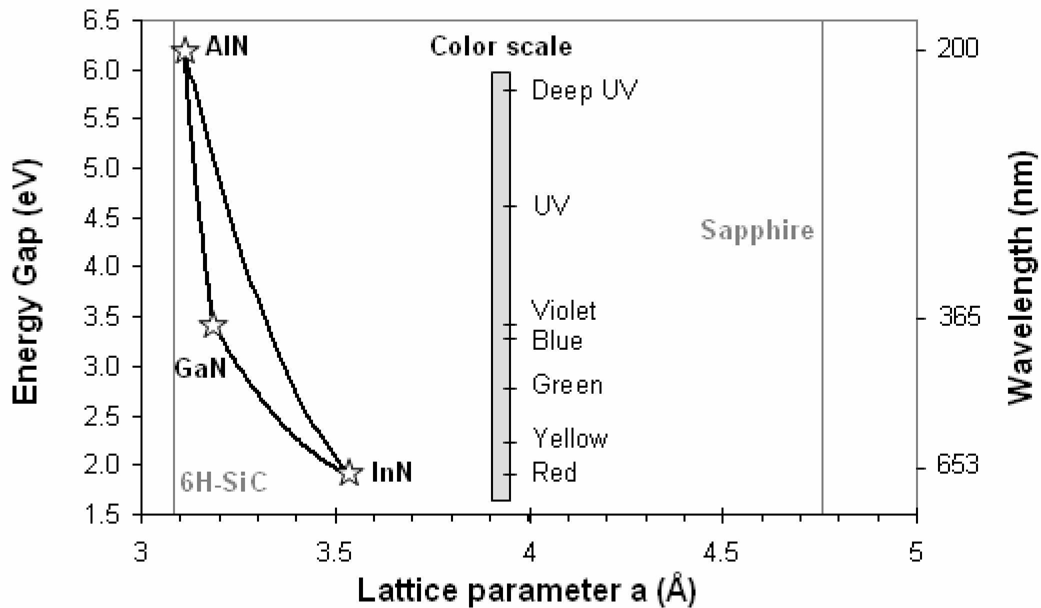

Figure 1.2: Bandgap versus a-lattice constant for the $In_xAl_yGa_{1-x-y}N$ system.

1.2 Motivation for III-Nitride Photodetectors

Photodetector arrays that can photon count are often required for detecting weak signals in low-background scenes. Examples of this include deep-space astronomy at infrared and visible wavelengths, and ultraviolet (UV) flame or plume detection at wavelengths near 280nm for terrestrial applications. Currently, most photon-counting systems operating in the solar-blind UV region use detectors based on photomultiplier tubes (PMTs). A solid-state solution could deliver important benefits in cost, size, and power.

Photodetectors based on III-N materials can potentially provide improved receiver sensitivity, low noise, and low dark current densities for short-wavelength radiation in the UV spectral region. However, for these detectors to compete with PMT technology, they need to have a very high sensitivity and, for optimal sensitivity, they should also operate in Geiger mode, requiring stable avalanche breakdown characteristics. PMTs offer high-sensitivity UV detection with a photocurrent gain as high as 10^6 [1]. The PMTs, however, generally require a high-voltage power supply (>1,200V) as well as a cooled photocathode and hence PMT systems are relatively large, expensive, bulky, and fragile. Ultraviolet-enhanced Si avalanche photodetectors (UVAPDs) can be used in UV detection systems, but they typically have higher dark currents (i.e., in the nA range) at 300 K, require expensive or complex filters for solar-blind operation, and have only demonstrated photon-counting operation down to λ~400 nm [2]. Wide-bandgap semiconductor *p-i-n* photodetectors, such as GaN *p-i-n* diodes, however, can exhibit "intrinsically" visible-blind operation and also can offer a high internal gain by avalanche multiplication, thus improving detection sensitivity. In addition, wide-bandgap APDs are

also capable of lower noise and faster response times compared with UV photodetector devices that employ photoconductive gain [3]. Group III Nitride UVAPDs also offer improved sensitivity performance over III-nitride photodiodes operating at zero bias in a photovoltaic mode [4,5].

To realize high-performance III-nitride detectors, especially those operating in avalanche, the nitride material quality plays an indispensable role. Currently, the lack of a convenient large-area lattice-matched substrate creates many problems in the epitaxial growth of quality III-nitride films. Most of the epitaxial growth of nitride films has been performed on basal plane (c-plane) sapphire substrates (α-Al_2O_3) because it is inexpensive and has a high thermal stability. However, there is a 10% lattice mismatch between the nitride epitaxial layer and the sapphire substrates. Developing and using a lattice-matched and thermally compatible substrate material for III-nitride epitaxial growth will greatly improve the device performance. In this work, our objective was to develop III-nitride avalanche photodiodes (APDs) with high gain. To achieve this goal, APDs have been grown on low-dislocation density substrates. Also, optimized dielectric passivation and processing techniques were used. A detailed study on APDs, including research context and description of research is presented in Chapter 4.

1.3 Motivation for III-Nitride Devices in Visible Optoelectronics

Recently, the development and commercial production of group III-nitrides have played a major role in high brightness light emitting diodes (LEDs) despite their high density of defect levels. Solid state lighting by means of LEDs is an opportunity to lower the prime energy consumption. III-nitride based material system has brought innovative

changes in photonic devices, which enable operating wavelengths to extend up to ultra-violet (UV) spectral region from green visible spectral region, which was previously covered by conventional gallium phosphide (GaP), gallium arsenide (GaAs), or indium phosphide (InP) semiconductor material systems. Because the extended wavelength covers blue visible spectral region as well, the emergence of III-nitride materials has made a tremendous impact on visible spectrum LEDs. Adding blue LEDs fills the missing spot of RGB (red-green-blue) primary color elements, which open up new opportunities for general white light illumination systems [6] and LED-based full color display systems. Figure 1.3 is a diagram showing energy bandgap of the III-V semiconductor materials for visible light emitting device applications.

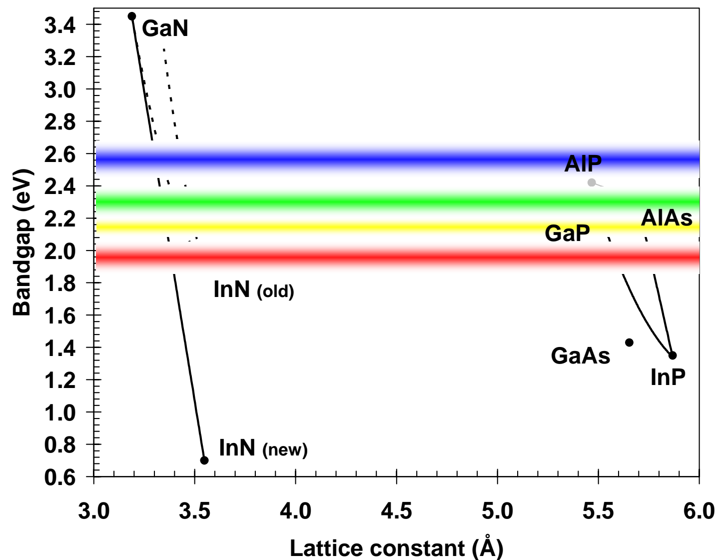

Figure 1.3: Energy gap vs lattice constant of III-V semiconductor materials for visible light emitting device applications.

While great success has been reported in the development of LEDs in the blue and violet spectral region (λ=390~480nm), less success has been demonstrated in obtaining high quantum efficiency [7] and low forward voltages (V_f) for LEDs operating in the visible green spectral region.

Some of the major obstacles to achieving high efficiency "green and longer wavelength" visible LEDs are: 1) achieving high indium composition in the active layers which are indium gallium nitride (InGaN) materials, 2) managing large lattice mismatch between buffer layers and active layers as indium composition increases, and 3) control of phase separation in InGaN materials, 4) low-damage mesa etching techniques, and 5) low-resistance Ohmic contacts to the *p*- and *n*-layers. For this project, the research objective was to develop visible LEDs emitting at "green and longer wavelengths" with low forward voltages and high efficiencies. Towards this goal, an active region friendly *p*-type layer has been developed. A detailed study on green LEDs, including a literature survey, is presented in chapter 5.

1.4 Motivation for III-Nitride Devices in Power Electronics

In the past decade, wide-bandgap nitride semiconductor materials have attracted increasing attention for high-power and high-temperature electronic devices [8,9]. Because of the strong polarity of the group III-nitride bond, the III-nitrides exhibit remarkable chemical, physical, and thermal properties. Furthermore, III-nitride materials possess some unique advantages, such as wide bandgap, high electron saturation drift velocity, high electric field strength, high thermal conductivity, and the possibility of lattice-matched heterostructure formation. All of these properties are crucial for the realization of recently emerging power electronic devices, which are required to operate at higher power levels, and in hostile environments.

There are many types of power electronic devices ranging from Schottky diodes, *p-n* junction diodes, heterostructure field effect transistors (HFET), heterostructure bipolar transistors (HBT), and thyristors that can be used to realize the power supply function of rectifying and switching. However, simple device structures, such as Schottky rectifiers and *p-i-n* rectifiers, are the most immediate means to exploit the superior properties and high-power handling capability of III-nitride materials. In addition, the study of these basic devices allows us to understand the fundamental material properties and to further explore the potential applications of more complicated devices.

The use of III-nitride materials in semiconductor power electronics has increased over the past decade because of the inherent advantages the material system offers. As mentioned previously, the high-saturated electron drift velocity along with the large breakdown field, give GaN advantages over Si, SiC and GaAs devices.

An overview of the critical material properties for these common materials used in electronic devices is given in Table 1.1. Even though SiC has a distinct thermal conductivity advantage, GaN can be grown on SiC substrates to take advantage of the superior thermal properties. SiC is also considered a competing candidate, yet GaN offers advantages over it as well. For instance, heterojunctions can be made using III-nitride based material system, which enables it to have a much higher current handling capability for lateral devices, such as HFETs.

Table 1.1: Si, GaAs, 4H-SiC, 6H-SiC and GaN material properties**.**

Material Property	**Si**	**GaAs**	**4H-SiC**	**6H-SiC**	**GaN**
Bandgap (eV)	1.12	1.42	3.265	3.023	3.40
Breakdown Field (10^5 V/cm)	3	4	18	22	35
Saturated Velocity (10^7 cm/s)	1	1	2	2	2.5
Electron Mobility ($cm^2/V{\cdot}s$)	1350	6000	800	800	1000
Hole Mobility ($cm^2/V{\cdot}s$)	450	330	120	120	20
Thermal Conductivity(W/cm·ºK)	1.5	0.46	4.9	4.9	1.3
Dielectric Constant ($\times \varepsilon_0$)	11.8	12.8	9.7	9.7	10.0

While taking advantage of the unique material properties, the objective of the gallium nitride (GaN)-based *p-i-n* rectifiers was to enable high-voltage devices with low on-resistances. The primary advantage of employing *p-i-n* rectifiers as power devices is to benefit from the low resistance during the "On-state" operation of such a rectifier. Thus, the device can sustain a high current density under forward bias with low power losses. These devices, like other III-nitride power devices, are expected to provide a new paradigm for space power switching applications and to enable a new generation of high-power and high-temperature switching electronics in space, leading to higher efficiency, lower cost, and lower weight space-based systems. Like other *p-n* junction devices described previously, the material quality and processing techniques will have a significant effect on the device performance. To achieve devices with high breakdown-voltages and low on-resistances, various growth and processing methods have been undertaken for *p-i-n* rectifiers. A detailed study on *p-i-n* rectifiers is presented in chapter 6.

1.5 Scope of this Dissertation

The work described in the present dissertation examines several possibilities available to improve the design, material quality, and fabrication of a few important III-nitride based *p-n* junction devices. These devices are APDs, Green LEDs and *p-i-n* rectifiers. In Chapter 2, the characterization methods for the materials and devices will be examined in detail. In Chapter 3, the basic operating principles of the relevant devices will be presented. In Chapter 4, the device structure, fabrication, and device performance of III-nitride APDs will be discussed. Chapter 5 focuses on the effect of different *p*-

layers on Green LED performance as well as LEDs emitting at longer wavelengths. Chapter 6 is devoted to the fabrication and characterization of high performance *p-i-n* rectifiers. Finally, Chapter 7 will provide a summary of this work.

CHAPTER 2

CHARACTERIZATION TECHNIQUES

2.1 Material Characterizations

This chapter will discuss several techniques that were used to characterize the structures, electrical properties, and optical properties of the *p-n* junction device structures. The main methods are X-ray diffraction, photoluminescence and cathodoluminescence, atomic force microscopy, scanning electron microscopy, secondary ion mass spectroscopy, hall-effect measurement, transmission line measurement, DC current-voltage measurement system and electroluminescence.

2.1.1 X-ray Diffraction

X-ray diffraction (XRD) is an essential tool for studying semiconductor materials, especially heterostructures, and thus, must be included in the study of devices involving homojunctions and heterojunctions. The prime purpose of the measurement is to determine the lattice constant of the epitaxial layers. Using these values, accurate calculation of the strain and composition of the heterojunction can be made. Additionally, information about the interface quality, tilt, and dislocation density can also be examined. The details about calculating material compositions using X-ray diffraction are described elsewhere [10]. This characterization technique is very important for the

optimization of crystal growth, material composition identification, and the qualification of device wafers.

2.1.2 Photoluminescence and Cathodoluminescence

In order to analyze the intrinsic material properties of the device layers used in the fabrication of electronic and photonic devices, powerful optical spectroscopic techniques are available. Akin to the laser excitation of photoluminescence (PL), cathodoluminescence (CL) uses a scanning electron microscope (SEM) to create a beam of electrons generated from a heated filament, which is focused on a sample through a series of magnetic lenses. The electron beam is then raster scanned across the film by magnetic deflection, and the secondary electrons provide a magnified "picture" of the layer. Secondary electrons are collected by a detector for imaging, and photons are captured by mirrors and associated optics, and fed into a spectrometer. Because the system is part of an SEM, both of these can be measured at the same time, and the advantage of CL over PL is the use of electrons that enhance the resolution and the ability to spatially characterize a given sample. Spatial resolution is routinely on the order of 0.1μ to 1μm.

By analyzing the wavelength dependence of the intensity as well as the peak position and width of this radiation, the material composition, relative material quality, and electronic properties can be understood. These measurements may be taken at both room-temperatures (RTPL or RTCL) and low-temperatures (LTPL or LTCL). The LTPL and LTCL measurements are useful for fairly weak signals as impurities and for thin layers, respectively. Cooling the sample to liquid nitrogen or liquid helium temperatures

has the effect of increasing the signal intensity, thereby allowing increased spatial resolution and also reduces electron beam damage to the sample in LTCL. The associated reduction in thermal broadening of the emission allows improved spectral resolution.

The sample surface is impinged upon by photons of higher energy than the bandgap of the semiconductor or by electrons creating excess electron-hole pairs (EHPs). These EHPs recombine giving off a characteristic photon spectrum. The resulting luminescence is captured and focused through a set of optics into a spectrometer that can separate light into individual wavelengths. Finally, these separated photons are measured by a photomultiplier tube (PMT), which gives an output current to a computer controlled measurement system.

The direct bandgap of III-nitride semiconductors offers the ability to see the luminescence of the bandgap and defects very easily. It is important to understand the differences between PL and CL to apply the acquired data effectively. In CL, surface effects are spatially-resolved more than in PL. However, a major distinction relates to the means of excitation. CL usually produces emission from all possible luminescence mechanisms available in the solid because, for an energetic electron, there are many different crystal de-excitation and scattering modes available for excess energy dissipation in the solid. Most of these processes contribute to electron-hole pair production in one capacity or another. The radiative recombination of electron-hole pairs (EHPs) leads to emission. An incoming high-energy electron must reduce its energy from tens of keV to zero energy. This dissipation process (for a single electron) can generate higher densities of "hot" electron-hole pairs (by many orders of magnitude) than

with PL. PL utilizes laser radiation with considerably lower excitation energies (photons having energies of several eV). Excitation may be resonant (selective excitation of specific emission process) or non-resonant. By comparison, each absorbed photon produces a single electron-hole pair. Another factor that may come into play is the charged nature of excitation: negatively charged electrons (CL) versus neutral photons (PL). The incoming fast electron represents an impulse of applied charge to the solid. The dielectric response of the solid is fundamental to physical interpretation. For instance, anomalous surface and bulk charging phenomena can occur with poorly conducting materials such as GaN on sapphire, especially when bombarded with low energy electrons (< 5 keV). Care must be taken to properly ground the samples.

Depth-resolved measurements are more easily performed with CL than with PL. Electron penetration depth can be readily varied by changing the accelerating voltage. The electron gun can provide accelerating voltages in the range $0.2 < V < 40.0$ kV, probe currents in the range $10^{-12} < I < 10^{-5}$ A, and magnifications in the range $10X < M < 300{,}000X$. On the other hand, wavelength tuning is severely limited with the argon-ion laser used for PL. Clearly, CL has a greater number of mitigating circumstances to contend with in comparison with PL.

A Gatan-Oxford CL system was used in the CL measurement, and features an integrated monochromator coupled directly to the collection optics within the SEM chamber. Light emitted from the sample is collected by a parabolic mirror and transmitted to the monochromator via a vacuum window. Adjusting mirrors in the monochromator either allows all the light to fall directly on the high-sensitivity detector, or be diverted through the entrance slits of the monochromator for spectral analysis and

subsequent monochromatic imaging. MonoCL2 software is controlled by Windows, and is fitted with a GaAs PMT.

2.1.3 Transmission Electron Microscopy

In principle, transmission electron microscopy (TEM) is very similar to optical microscopy. The resolution of TEM can be estimated by the following equation,

$$s = \frac{0.61 \cdot \lambda}{NA} \tag{2.1}$$

where NA is the numerical aperture and λ is the electron wavelength. Consequently, TEM method can give resolutions as small as 2 Å. Due to its extremely high-resolution capability, TEM was originally used for highly magnified sample images. Later, analytical TEM came of age as electron energy loss detectors, and X-ray detectors were added to the instrument, and the technique now becomes an extremely powerful tool to characterize the structural properties of materials down to the atomic level [11].

When an electron beam is incident on the sample, several interactions between the electron and the sample can occur. If the electron does not strike an atom in the sample, it will continue to travel in a straight line until it reaches the detector. If the electron does come into contact with the sample, it can either bounce off elastically without any loss of energy, or inelastically, transferring some of the energy to the atom. In an inelastic interaction, the amount of energy conveyed from electron to sample is variable and random. Therefore, inelastic scattering, leading eventually to absorption, must be avoided since it contains no information and generates noise in the image. Meanwhile, if the electron undergoes elastic scattering, the energy remains constant, and the law of

conservation of momentum will determine the angle at which it will be reflected. Thus, the diffraction contrast arises when there is interference between electrons coming in from different angles. Electrons that interact with the sample are bent away from their original path, and will interfere with the main electron beam. For material crystallographic information purposes, diffraction contrast is the most useful technique. Diffraction contrast can be used to study various lattice defects such as dislocations, stacking faults, etc.. The correct interpretation of TEM images usually requires simulations, using dynamical diffraction theory.

High-resolution TEM characterization and TEM sample preparation of the samples were performed at Lawrence Berkeley National Laboratory by Dr. Z. Liliental-Weber.

2.2 Surface Characterizations

2.2.1 Atomic Force Microscopy

Atomic force microscopy (AFM) makes use of a microscopic metal or semiconductor tip to probe the surface features of a film. Its ability to provide a high resolution map of the surface morphology both laterally and vertically makes it useful for looking at small features and defects that other characterization tools may miss.

The principle of operation is based on the measurement of the deflection of the tip and cantilever using reflected laser light and a photodetector. There are three distinct modes that can be used to study the sample surface, which are contact mode, non-contact mode, and tapping mode. In contact mode, the tip is simply dragged across the surface, but this can damage both the tip and the sample. In non-contact mode, the tip is kept a

constant distance from the surface, and the force required to keep it there is mapped. However, this results in poor resolution. Lastly, so-called tapping mode was proposed, which combines the two previous techniques and vibrates the cantilever at its resonant frequency. By doing this, an increase in sensitivity by several orders of magnitude was obtained because the local gradient van der Waals forces induce a change in the frequency, phase, and amplitude, which is fed back into the system [12].

In this manner, surface features on the order of ~100 Å can be resolved. AFM is useful for measuring the surface roughness of epitaxial layers and to understand the nature of defects in the layers. The AFM tool used in this study was a Veeco Dimension 3100, operating in tapping mode.

2.2.2 Scanning Electron Microscopy

The SEM was described above in the section relating to CL. It is used to record high-resolution images of processed device structures and metal layers to give a measure of process quality and uniformity. It is also useful for identifying surface morphology and defects along etched sidewalls. The SEM photographs used in this dissertation are taken from JEOL 6400FV and Hitachi 3500H.

2.2.3 Secondary Ion Mass Spectroscopy

Secondary ion mass spectroscopy (SIMS) is a common technique used for measuring the atomic concentration in a layer. SIMS is sensitive down to the ~ 10^{16} cm^{-3} concentration range for most atoms. SIMS is a destructive technique because an ion beam (usually Cs^+) is used to displace atoms from their lattice sites. The displaced atoms

or ions are collected and analyzed by a mass spectrometer that identifies the particles. In this manner, the composition of the film can be determined. When coupled with sputtering, SIMS can be used to generate atomic profiles as a function of depth. This technique is very useful for determining dopant and impurity profiles.

2.3 Electrical Characterizations

2.3.1 Hall Effect

The Hall effect measurement is a very simple technique for characterizing semiconductor material resistivity, carrier concentration, carrier type, and carrier mobility. The Hall effect occurs when an electromagnetic field is applied across a biased conductor, which produces a potential difference in the plane orthogonal to the magnetic field [34]. The ratio of the measured voltage to the product of the current and magnetic field is defined as the Hall-coefficient (R_H), which is inversely proportional to the charge carrier density by,

$$n = \frac{1}{-qR_H} \quad \textbf{or} \quad p = \frac{1}{qR_H} \tag{2.2}$$

This technique was further developed by L. J. van der Pauw, and was applied on an arbitrarily shaped flat sample with four points on the circumference of the shape. According to van der Pauw's theorem, the resistivity is given by,

$$\rho = 1.1331\left(\frac{t}{I}\right)\left(\frac{f_1\Delta V_1 + f_2\Delta V_2}{2}\right) \tag{2.3}$$

where t is the thickness of the film, I is the applied current, ΔV_i is the voltage drop across the sample in various configurations, and f_1 and f_2 are the geometrical factors (that are unity for perfect squares).

Similarly, the relationship of the mobility μ to the magnetic field B is given by,

$$\mu = 2.5 \cdot 10^7 \cdot \left(\frac{t}{I \cdot B \cdot \rho} \right) \cdot \left(\frac{\Delta V_3 + \Delta V_4}{2} \right) \tag{2.4}$$

and the bulk carrier concentrations as functions of mobilities and the resistivities are given by,

$$n = \frac{1}{\rho \cdot q \cdot \mu} \text{ for n-type material or } p = \frac{1}{\rho \cdot q \cdot \mu} \text{ for p-type material} \tag{2.5}$$

Furthermore, temperature-dependent Hall-effect measurements are employed in determining the nature of the dopants in homogenous semiconductor layers.

2.3.2 Transmission Line Measurements

The transmission line measurement (TLM) has been widely used for Ohmic contact analysis for device characterization because of its simplicity and accuracy. The TLM method employs an etched mesa, and metal contact pads are subsequently deposited on the top of the mesa as shown in Figure 2.1. Figure 2.1 illustrates some parameters used in the measurements and calculations: L_t = transfer length (μm), L = length of rectangular contact (μm), Z = width of rectangular contact (μm), d = spacing between contacts (μm). The purpose of the mesa is to confine the current flow to the area between contact pads.

An important parameter that indicates the quality of the Ohmic contact is the specific contact resistance, also called the contact resistivity. The specific contact resistance is an interfacial parameter equal to the product of the contact resistance and the effective area of the contact through which current flows. By measuring the resistance

between the two contact pads, and plotting as a function of *d*, the contact resistance can be extrapolated, as shown in Figure 2.2.

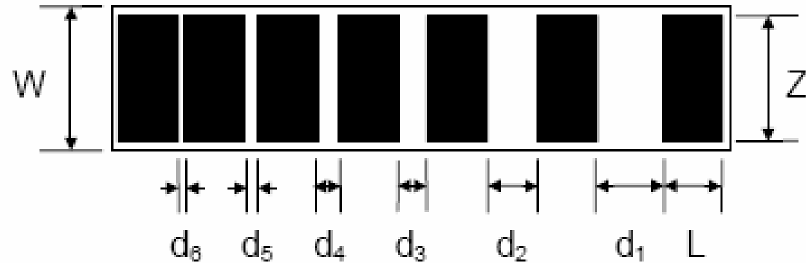

Figure 2.1: Plain view of the TLM pattern showing the semiconductor mesa with dark metal pads.

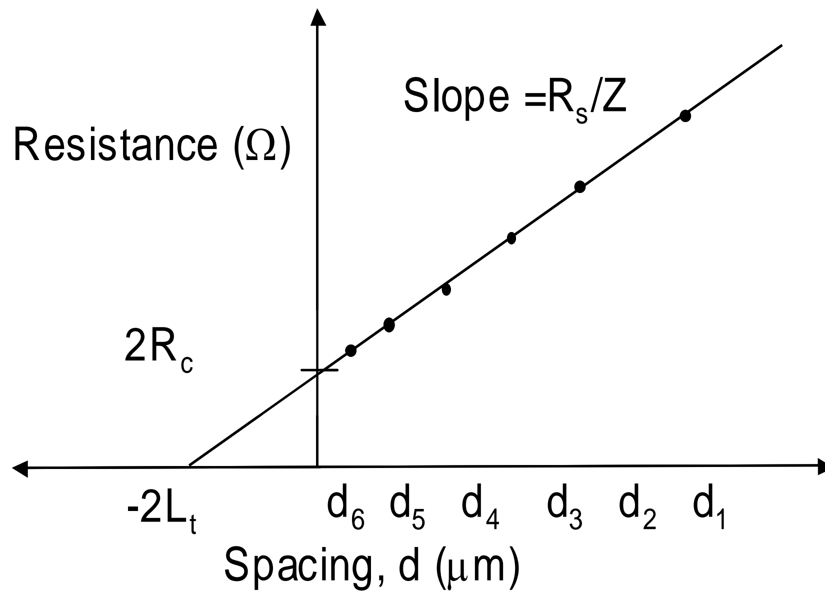

Figure 2.2: Plot of measured resistance versus contact spacing.

The sheet resistance of the semiconductor can be calculated from the slope where,

$$R_s = slope \cdot Z \tag{2.6}$$

As shown in Figure 2.2, the *x*-intercept is twice the transfer length, $2L_t$. The transfer length is defined as the distance from the edge of the contact pad to the point at which the contact voltage is *1/e* of its maximum value. The *y*-intercept gives twice the contact resistance, $2R_c$. The effective contact area is defined as the product of the transfer length and the contact width ($Lt \times Z$). The specific contact resistance can then be calculated from the following equations:

$$\rho_c = L_t \cdot Z \cdot R_c \tag{2.7}$$

$$R_c = \frac{R_s \cdot L_t}{Z} \tag{2.8}$$

2.3.3 DC Current-Voltage Measurements

The DC characterization of the devices is conducted on a probe station, which is fitted with three tungsten probes. These are then connected to a Hewlett-Packard (HP) 4146C DC Source/Monitor controlled by a computer via a GPIB interface. Interactive Characterization Software's Metrics® software is programmed to ramp and measure voltage and current levels to generate curves for devices.

2.3.4 Electroluminescence

Electroluminescence (EL) measurements are an indispensable technique to characterize the spectral properties of the optical devices. In an LED, EL is the process

of radiative recombination resulting from excess carrier injection into the *p-n* junction active region. The EL spectroscopy system mainly consists of a power supply, a spectrometer and a signal acquisition unit. A DC current source is used to supply current to the devices. For ultra-violet (UV) LEDs, our EL system consists of SPEX 500M spectrometer and SpectrAcq2® acquisition system. It is fully controlled by a computer using SPECTRAMAX 3.0 software, used for measurements and data acquisitions. For visible LEDs, an Ocean-optics EL system was used. It consists of HR2000 Composite-grating, 2048-pixel CCD Linear Image Sensor and 400 micron-fiber, controlled by Labview software.

CHAPTER 3

OPERATING PRINCIPLES OF RELEVANT DEVICES

3.1 Introduction

This section discusses the operating principles of *p-n* junction devices that are described in the later chapters. Three types of devices will be described in this chapter – *p-i-n* photodetectors, light emitting diodes (LEDs) and *p-i-n* rectifiers.

In a *p-i-n* photodetector, the incoming photons are absorbed in *i*-region, which generates electron-hole pairs (EHPs). These EHPs can be swept by the built-in field in the drift region and contribute to a photo-current. In an LED, electrons are injected from the n-side and holes are injected from the p-side, to recombine in the active region. While the recombination can occur through many different mechanisms, in a direct bandgap material, the probability is high that the recombination will occur through an optical process, yielding one photon per recombination. In a *p-i-n* rectifier, the drift layer or *i*-layer is a lightly doped region, which can support a large voltage under reverse-bias operation. It also takes advantage of the low resistance during the "On-state" operation of the diode in forward-bias operation.

3.2 PIN Photodetectors

A *p-i-n* photodetector is a junction diode that produces current under excitation by photons of appropriate wavelength. Under reverse bias conditions, the current carried by the device is limited by the availability of electrons in the *p*-layer and availability of holes

in the *n*-layer. Normally, these are limited by the thermal generation rate within the depletion region and a few diffusion lengths on both sides of the depletion region. The generation rate is quite low, particularly for wide-bandgap semiconductors at room temperature.

Semiconductor materials can absorb the energy of a photon by the transition of an electron from the valence band to the conduction band (generation of an EHP). For band-to-band transitions, the minimum energy that the photon is required to have equals the bandgap energy of the semiconductor. Thus, if a *p-n* junction is illuminated with photons of energy equaling or exceeding the bandgap energy, an EHP is generated for each photon absorbed; and carriers can be swept away according to the direction of the electric field in the depletion region and this carrier can contribute to the reverse current. This mechanism can be used for photodetection.

For a given semiconductor on which photons of a given energy are incident, the photon has a certain probability of absorption within a unit length. This probability is characterized by an absorption rate per unit length – given by the absorption coefficient α. Considering only a band-to-band absorption, the absorption rate becomes non-zero at the bandgap energy and goes up fast for higher-energy photons. For a simple *p-n* diode, the length over which photogeneration occurs is small and the absorption of a significant part of the photon does not occur over this small length. As a result, a *p-i-n* diode with an optimal *i*-layer thickness is used.

For a photodetector, an important quantity is the external quantum efficiency (EQE) at a given wavelength. The absorption of incident photons in the un-depleted *p*- and *n*-layers is an undesirable effect in a photodetector because the carriers excited in

these regions do not contribute to the photocurrent and act to reduce the EQE. It is desirable to introduce all the incident photons directly at the *i*-region. This is possible by the use of heterostructures. If the *p*- and *n*-type regions are made of wider-bandgap material, they will be transparent to the photons to be absorbed in the *i*-layer. However, if the device is designed this way, the photodetector will not be sensitive to photons of energy larger than the bandgap energy of the wider bandgap material because those photons will be strongly absorbed in the bulk. Often, detection of photons of much higher energy than the bandgap of the *i*-layer is required. Since at this much higher energy, the absorption coefficient is very large, only a very thin *i*-layer is used. Also, the thickness of the bulk layer on the illumination side has to be kept small. One example of this is the design of the UV-enhanced Si photodetector.

Another mode of operation in a *p*-*i*-*n* diode is in the avalanche regime. In this regime, one incident photon can create a number of EHPs by the avalanche multiplication process. Since each photon can create multiple carriers, a very high EQE can be obtained. This amplification is known as avalanche gain. For operation in the avalanche mode, *i*-layer thickness is to be selected such that the built-in field under desired reverse bias voltage equals the breakdown field. The research on *p*-*i*-*n* detectors for this work was focused on avalanche mode.

Similar to the technique of light extraction in LEDs, simple optical considerations can increase the EQE for photodetectors. For example, at each interface of different refractive index in the light path towards the absorption region, Fresnel reflection occurs, which reduces the photon flux actually reaching the absorption region. This problem can be partially solved by using anti-reflective coatings.

In addition to these basic features, many other issues have to be taken into account to improve the performance of photodetectors. For example, the junction capacitance and series resistance should be minimized in order to reduce the *RC* time constant for improved speed. More details on the operation of *p-i-n* photodetectors can be found in various textbooks on electronic and optoelectronic devices [13], [14].

3.3 Light-Emitting Diode Basics

3.3.1 Injection Luminescence and Radiative Recombination

An LED is simply a semiconductor *p-n* junction diode that emits light upon the application of a forward bias. This luminescence mechanism is called electroluminescence and light from the ultra-violet to the infrared regions of the spectrum can be obtained depending on the semiconductor material.

When a forward voltage is applied across a *p-n* junction, minority carriers are injected across the junction to establish excess carriers above their thermal equilibrium density. The excess minority carriers recombine with the majority carriers, and energy is released in the form of heat (phonons) or light (photons). The process is illustrated in Figure 3.1. The recombination of electrons and holes in a semiconductor can either be radiative or non-radiative. In LEDs, there is competition between radiative and non-radiative recombination, and clearly we need to enhance the radiative process while minimizing the non-radiative process. The parameter used to characterize the recombination process is the recombination lifetime, t.

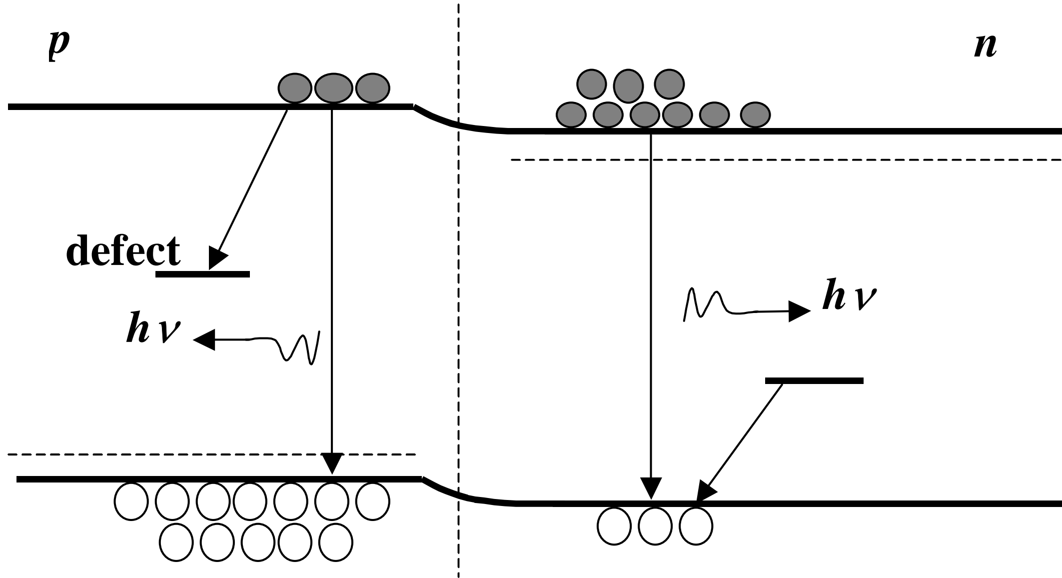

Figure 3.1: Schematic band diagram of an electroluminescent *p-n* junction under a forward bias condition.

The recombination lifetime consists of both a radiative lifetime, t_r, and non-radiative lifetime, t_{nr}, and is given by,

$$\frac{1}{t} = \frac{1}{t_r} + \frac{1}{t_{nr}} \tag{3.1}$$

The probability of radiative recombination or internal quantum efficiency can be expressed in terms of the radiative and non-radiative lifetime as,

$$\eta_i = \frac{\frac{1}{t_r}}{\frac{1}{t_r} + \frac{1}{t_{nr}}} \tag{3.2}$$

3.3.2 External Quantum Efficiency

After photons are generated at the *p-n* junction, they must pass through the crystal to reach the surface. Some of the emitted photons are reabsorbed by the semiconductor during this process. Furthermore, even after the photons have reached the surface, they may not be able to escape from the semiconductor due to the large difference in the refractive indices between the semiconductor and air. One of the important measures for LED performance is its external quantum efficiency. The external quantum efficiency is product of material and optical coupling efficiency given as [15],

$$\eta_{ext} = \eta_{inj} \cdot \eta_i \cdot \eta_{opt} \tag{3.3}$$

where η_{inj} is the injection efficiency, η_i is the internal quantum efficiency as described previously, and η_{opt} is the light extraction efficiency.

3.3.3 Emission Spectrum

Spontaneous recombination is the dominant mechanism in the LED photon emission process. Nitride LEDs has its own unique optical emission spectrum characteristics.

Assuming the electrons in the conduction band and the holes in the valence band have parabolic dispersion relations, the joint density of states can be calculated as,

$$\rho(E) = \frac{1}{2\pi^2}\left(\frac{2m_r^*}{\hbar^2}\right)^{3/2}\sqrt{E - E_g} \tag{3.4}$$

where m_r^* is the reduced effective mass.

The distribution of carriers in the allowed energy bands is governed by the Boltzmann distribution,

$$f_B(E) = e^{-E/(kT)} \tag{3.5}$$

Therefore, the emission intensity as function of energy is proportional to the product of Equations 3.5 and 3.6,

$$I(E) \propto \sqrt{E - E_g} \cdot e^{-E/(kT)} \tag{3.6}$$

3.3.4 Heterostructures

One of most important improvements in LED structure design is the incorporation of a double-heterostructure (DH) instead of a homojunction device. In this design, the lower-bandgap lightly doped or intrinsic material is sandwiched between wider-bandgap *p* and *n* material. The use of a double-heterostructure can solve two of the main problems associated with a homojunction structure [16]. First, the DH leads to an increased minority carrier injection efficiency due to the band-offset. Second, the wide-bandgap material in the heterostructure is transparent to the light generated in the narrow-gap active layer and therefore does not contribute to photon reabsorption. Both factors help to increase the overall device quantum efficiency.

3.4 PIN Rectifiers

One of the advantages of *p-i-n* rectifiers over Schottky barrier rectifiers or other *p-n* junction diodes is their capability to support a higher reverse voltage. The device structure consists of a lightly doped epitaxial drift layer of thickness *W* (*n*-type or *p*-type)

sandwiched between two thin heavily doped epitaxial layers of opposite conductivity. The advantages of utilizing the *p-i-n* structure instead of usual *p-n* junction structure can be illustrated in Figure 3.2. The Figure shows the doping distribution and electrical field distribution for normal *p-n* and punch-through *p-i-n* diode.

The breakdown voltage of the punch-through *p-i-n* diode is simply the area under the $\varepsilon(x)$ versus x trapezoid. From this Figure, we can tailor the doping of the i-region to make the checked area equal to the grey area, meaning that both diodes could sustain the same breakdown voltage. It implies that a diode with much narrower base could achieve a desired breakdown voltage in the *p-i-n* punch-through diode compared to a *p-n* junction device. This has important advantages in terms of both current conduction and processing convenience.

This device structure also offers extremely low leakage current in the reverse bias regime. The total reverse leakage current for a *p-i-n* rectifier with *n*-type drift region is given by [17],

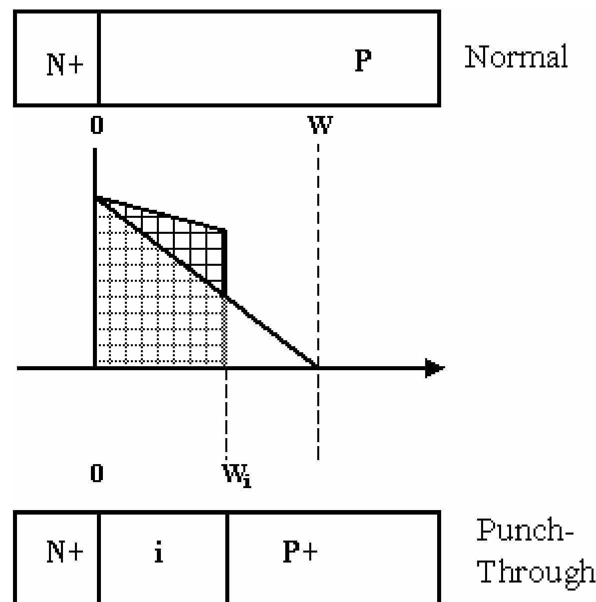

Figure 3.2: Comparison of punch-through diode structure with normal *p-n* junction diode.

$$J_L = J_{DP} + J_{SC} + J_{DN}$$
$$= \frac{qD_n n_i^2}{L_n N_A} + \frac{qWn_i}{\tau_{sc}} + \frac{qD_p n_i^2}{L_p N_D} \tag{3.7}$$

where J_{DP} is the diffusion current component from the $p+$ region, J_{SC} is the space charge generation current from the depletion region, and J_{DN} is the diffusion current component from the $n+$ region. $D_{n,p}$ is the diffusion coefficient for electrons and holes, $L_{n,p}$ is the diffusion length of electrons and holes, $N_{A,D}$ is the carrier concentration in $p+$ and $n+$ regions respectively. Also, n_i is the intrinsic carrier concentration, W is the thickness of the *i*-region and τ_{sc} is the space charge generation lifetime.

3.4.1 Forward Conductivity Modulation

By proper design, the *p-i-n* device could provide a low forward voltage due to the conductivity modulation of the drift region. The forward voltage drop of a *p-i-n* rectifier consists of the drop across the *i*-region (V_i) and the drop across the left and right junctions (*p+/i* and *n+/i*) and is given by,

$$V_F = \frac{kT}{q} \ln\left(\frac{n^- n^+}{n_i^2}\right) + V_i \tag{3.8}$$

where n^- and n^+ are the electron concentrations at the two end regions.

The on-state characteristics of an ideal *p-i-n* diode can be described in closed form by the relationship,

$$J_F = \frac{4qD_a n_i}{W} F\left(\frac{W}{2L_a}\right) \exp(qV_F / 2kT) \tag{3.9}$$

where $$F\left(\frac{W}{2L_a}\right) = \frac{\left[\left(\frac{W}{2L_a}\right)\tanh\left(\frac{W}{2L_a}\right)\right]}{\sqrt{1-\frac{1}{4}\tanh^4\left(\frac{W}{2L_a}\right)}}\exp(-qV_F\,/\,kT) \qquad (3.10)$$

D_a is the ambipolar diffusion coefficient, L_a is the ambipolar diffusion length and W is the thickness of the drift region. The function $F(W/2L_a)$ has a peak when $W/2L_a=1$. This would indicate that the forward voltage drop is minimized at this point. It falls as the $W/2L_a$ increases [18]. The condition $W=2L_a$ thus characterizes the conductivity modulation of the *p-i-n* junction rectifier. As $W \geq 2L_a$, the voltage drop across *i*-region can be relatively high and the required breakdown voltage typically determines the thickness of *i*-region. To utilize conductivity modulation in the *p-i-n* structure, L_a must be kept large. However, the carrier-carrier scattering effect serves to reduce the ambipolar diffusion coefficient D_a with increased injection of carriers. The minority carrier lifetime τ will also be reduced because of Auger recombination processes at high carrier concentrations. Therefore, the $W/2L_a$ ratio will increase under high injection conditions. These effects are particularly significant when the carrier concentration is high.

CHAPTER 4

III-NITRIDE AVALANCHE PHOTODIODES

4.1 Introduction

Wide-bandgap semiconductor *p-i-n* photodetectors, such as III-Nitride *p-i-n* diodes, can exhibit "intrinsically" visible-blind operation, and can also offer a high internal gain by avalanche multiplication, offering high detection sensitivity. Wide-bandgap semiconductor *p-i-n* UV photodiodes with high avalanche gain have been reported based on SiC epitaxial layers grown on SiC substrates [19,20,21], with a recent publication reporting 100 μm-diameter 4H-SiC separate-absorption-multiplication (SAM) APDs having gains as high as 1,000 [20].

The development of GaN-based APDs, however, has been hampered by high dislocation densities in the epitaxial layers grown on lattice-mismatched substrates and only a few reports have been made of true avalanche gain in heteroepitaxial GaN-based APDs [22,23,24,25]. For these previous reports, the GaN *p-i-n* devices were ~30-37 μm diameter and the optical avalanche gain was low ($8<M<300$) [23, 25,26]. The high density of defects and dislocations commonly observed in heteroepitaxial III-N *p-i-n* APDs grown on sapphire or SiC can lead to a premature microplasma breakdown in the active region of the detector before the electric field in the depletion region can reach the bulk avalanche breakdown field.

To minimize the dislocation density of the devices, the growth of GaN-based *p-i-n* avalanche photodiodes on low-dislocation density (~10^5-10^6 cm^{-3}) *n*-type "bulk" GaN substrates [27] have been undertaken, by metal-organic chemical vapor deposition

(MOCVD). Another issue for preventing avalanche in GaN-based APDs is the sidewall leakage current. The plasma damage during mesa formation of the device can cause excess leakage current through the sidewall. To minimize this, a low-damage etching technique, as well has a high-quality dielectric passivation are required.

4.2 GaN Avalanche Photodiodes

The GaN epitaxial materials used in this study were grown by metal-organic chemical vapor deposition (MOCVD) using a Thomas Swan reactor system [28] equipped with a Close-Coupled Showerhead (CCS) growth chamber. Hydrogen (H_2) was used as the carrier gas mixed with ammonia (NH_3) as a hydride precursor and with EpiPure^{TM} [29] trimethylgallium (TMGa) as the primary alkyl precursor. Silane (SiH_4) and bis-cyclopentadienyl magnesium (Cp_2Mg) were used as *n*- and *p*-type dopant precursors, respectively. The growth conditions for epitaxial layers were optimized to achieve improved crystalline and structural quality by altering the growth parameters. The device structures consist of a 2.5-µm thick *n*-type GaN:Si$^+$ layer, followed by a 0.3-µm thick, unintentionally doped (estimated n=5×10^{16} cm^{-3}) GaN *i*-type drift region, and topped with a 0.1-µm *p*-type GaN:Mg$^+$ layer. The typical layer structure of the GaN *p-i-n* devices is shown in Table 4.1.

Table 4.1: Composition, doping, and thickness of the layers of a GaN APD.

Layer	Composition	Thickness	Doping
p-contact	GaN:Mg^{++}	20 nm	[Mg] = ~2×10^{20} cm^{-3}
p-layer	GaN:Mg$^+$	0.1 µm	p = 1×10^{18} cm^{-3}
i-layer	GaN:ud	0.3 µm	n = 5×10^{16} cm^{-3}
n-layer	GaN:Si$^+$	2.5 µm	n = 5×10^{18} cm^{-3}
Substrate	Bulk GaN	~450 µm	n ~ 5×10^{18} cm^{-3}

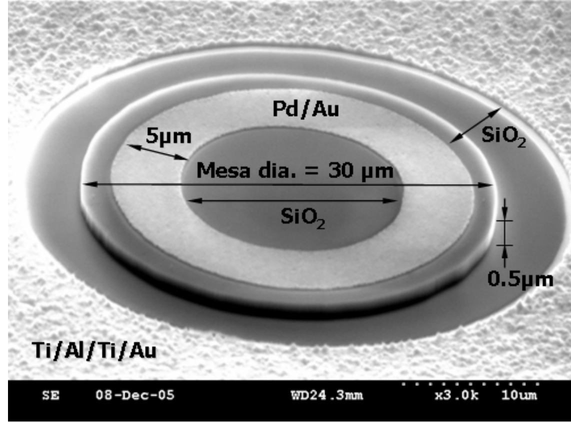

Figure 4.1: SEM image of a fabricated 30μm-diameter GaN APD device.

The electrical properties of the GaN:Mg layer, including the free-hole concentration, mobility, and electrical resistivity, were measured for GaN films produced under various growth conditions. The 300 K free-hole concentration in the *p*-layer was estimated to be $p{\sim}1\times10^{18}$ cm^{-3} as determined by Hall-effect measurements carried out for *p*-GaN:Mg layers grown on undoped GaN/sapphire substrates. The same growth conditions on undoped GaN/sapphire substrates were applied to the UVAPD structures grown on GaN substrates in this study.

The devices were processed into 30 μm- and 50 μm-diameter circular mesas by inductively coupled plasma (ICP) etching using a Cl_2/He carrier gas mixture. After mesa definition, a SiO_2 passivation layer was applied to the devices using plasma-enhanced chemical vapor deposition. Ti/Al/Ti/Au and Pd/Au Ohmic contacts were evaporated on the *n*-layer and *p*-layer, respectively, and annealed at 600˚ C in a nitrogen (N_2) ambient. The width of the ring-shaped *p*-contact metal is 5 μm. A scanning electron microscope (SEM) image of a fabricated device with a 30 μm-diameter mesa is shown in Figure 4.1. No attempt to taper the mesa-wall edge profile was made.

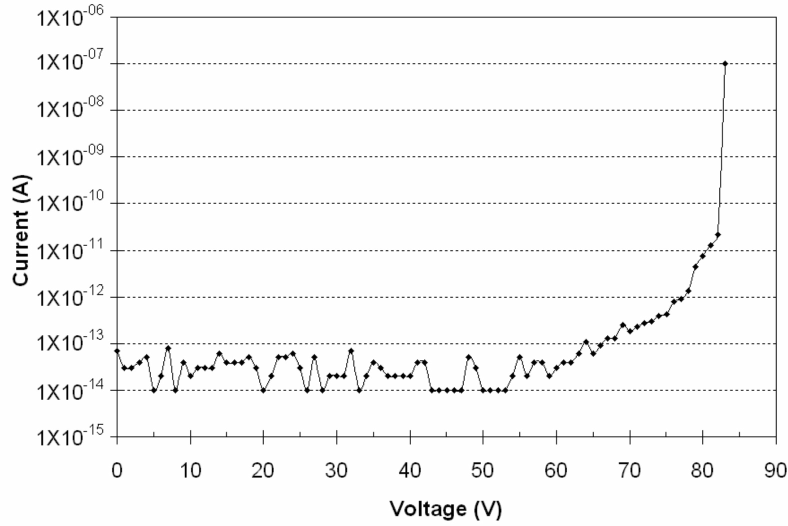

Figure 4.2: Reverse-bias dark-current characteristics of a GaN APD having a circular mesa of 30 μm diameter, showing a low dark current and current density of 2×10^{-11} A and 3.5×10^{-6} A/cm^2 respectively, just before avalanche breakdown.

Typically, the reverse-bias breakdown voltage, V_{BR}, of the 30 μm-diameter devices was between 80 V and 90 V, as measured on a probe station by an Agilent Model 4156C Semiconductor Parameter Analyzer. Figure 4.2 shows the reverse-bias current-voltage (I-V) characteristics of a 30 μm-diameter mesa device measured in the dark, showing an instrument-limited low-reverse-voltage ($|V_R|$<60V) dark current and current density of I_R=5×10^{-14} A and J_R=7.0×10^{-9} A/cm^2, respectively, and values of I_R=2×10^{-11} A and J_R=2.8×10^{-6} A/cm^2 at V_R~-82V, just before breakdown. To confirm avalanche breakdown, the temperature-dependent reverse-bias I-V characteristics were measured. The magnitude of the reverse-bias breakdown voltage, $|V_{BR}|$, showed a clear positive increase with an increase in temperature. For temperatures of 313 K, 333 K and 353 K, the corresponding values of $|V_{BR}|$ were 86 V, 87 V, and 88 V, respectively. From this, we can estimate the temperature coefficient of the breakdown voltage to be ~0.05 V/K. The

positive temperature dependence of the magnitude of the breakdown voltage confirms that the abrupt increase in reverse current is predominantly due to avalanche effects and not by premature junction breakdown resulting from microplasmas or mesa-sidewall leakage paths. In addition, multiple reverse-bias *I-V* scans (~40 times) show consistent breakdown voltage and leakage current characteristics at room temperature.

Figure 4.3 shows a comparison of the photocurrent and dark-current characteristics at 300K for a 50 μm-diameter mesa UVAPD. No microplasma or edge breakdown emission was visually observed, and many of the tested devices rolled into breakdown consistently (for over 40 scans) over all wavelengths (280 nm ~ 365 nm) tested, suggesting that no microplasmas were formed. Therefore, edge gain and microplasma-related gain are not considered in the calculation of the avalanche gain for these devices. The data in Figure 4.3 were obtained using a UV lamp-monochromator combination operating at a peak emission wavelength of ~360 nm and a spectral width of ~3 nm.

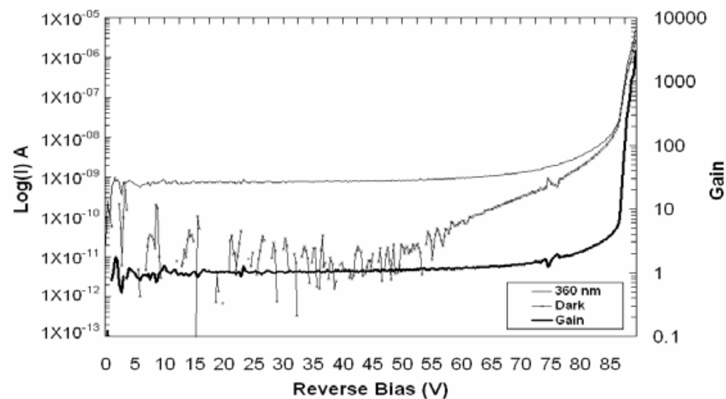

Figure 4.3: Reverse-bias *I-V* characteristics of a GaN APD having a mesa diameter of 50 μm. The dark current, photocurrent, and avalanche gain (*M*) are plotted versus reverse bias voltage. The diode shows gain in excess of *M*~10 at the onset of avalanche breakdown (-86.5 V, electric field of ~2.8 MV/cm), reaching a maximum avalanche gain greater than ~3,000.

The avalanche gain (M) is taken as the difference between the reverse-biased photocurrent and dark current, divided by the difference between the low-bias photocurrent and low-bias dark current. The low-bias currents are taken from the flat portion of the *I-V* curves for reverse voltages less than 60 V. In this low-applied-bias regime ($|V_R|<60V$), the difference between the photocurrent and dark current can be approximated as the photocurrent since the dark current is significantly lower. The photocurrent is almost constant without soft breakdown for the low-reverse-bias regime and is used as the normalization factor for calculating avalanche gain, i.e., as the unity-gain photocurrent. The device in Figure 3 exhibits an avalanche gain of over ~10 at the onset of breakdown of V_{BR} = -86.5V (electric field ~2.8 MV/cm), reaching a maximum avalanche gain greater than 3,000 [30], limited by the testing equipment. To the best of our knowledge, this is the first demonstration of true avalanche gain greater than 1000 achieved for photodiodes based on the GaN material system and it compares favorably with the gain of ~1,000 reported for a 100 μm-diameter SiC separate-absorption-and-multiplication (SAM) APD [31]. We believe this very high gain for this relatively large-area GaN UVAPD is partially attributable to the low defect density of the material; however, the fact that these devices exhibited stable avalanche breakdown in spite of the relatively sharp vertical sidewalls suggests that the low plasma-induced etch damage of the mesa and the high-quality dielectric passivation also played a role.

4.3 Dielectric Effects on the Performance of Avalanche Photodiodes

In this section, the effects of different dielectric passivations on the performance of GaN APDs were studied. The dielectrics used for passivations are silicon-dioxide

(SiO_2) and silicon-nitride (SiN). Different dielectric depositions were carried out on GaN APD structures grown on *n*-type 6H-SiC substrates. Because the focus of this study was to compare the effects of different dielectrics, fabrication was carried out on device structures with 6H-SiC substrates. The growth of GaN on an *n*-type 6H-SiC, a less lattice-mismatched material compared to growth on Sapphire, is another way to reduce the dislocation density and thus improve device performance with low cost. Also, SiC has a better thermal conductivity compared to sapphire. Therefore, as an alternative to reducing the dislocation densities, GaN *p-i-n* diode structures were grown on *n*-type 6H-SiC substrates. Compared to free-standing GaN substrates or semi-insulating 4H-SiC substrates, *n*-type 6H-SiC substrates are a more economical choice at this time.

Although the dielectric strength for SiN is similar to that of SiO_2 ($\sim 10^7$ V/cm), SiN passivation has been used extensively for state-of-the-art III-Nitride based electronic devices, showing its potential as a high quality dielectric passivation layer for III-Nitride based devices, which require high-voltage operations. Despite this, there have not been many reports on high performance III-Nitride based detectors using SiN dielectric layers. The refractive index for SiN is higher than that of SiO_2. However, the consequences of this as anti-reflective coatings for III-Nitride based detectors are not well known.

The device structure was identical to a GaN APD structure grown on GaN substrates, mentioned in the previous section [30]. X-ray diffraction (XRD) rocking curve and atomic force microscopy (AFM) analyses were employed to characterize the properties of the epitaxial structures as well as the GaN substrates prior to growth. The XRD rocking curve of the material showed line-widths of 351 and 403 arcsec for (002) and (102) scans respectively. The AFM image of the surface of a GaN UVAPD wafer

revealed atomic steps on the surface with no visible nano-pits and an rms roughness value ~0.196 nm for 1×1 μm^2 scan and ~0.307 nm for 5×5 μm^2 scan respectively, with a *z*-height scale of 20 nm. The devices were processed into 30 μm-diameter circular mesas by inductively coupled plasma (ICP) etching using a Cl_2/He carrier gas mixture. After mesa definition, SiO_2 and SiN passivations were applied to the devices using plasma-enhanced chemical vapor deposition. Both dielectric depositions were carried out at 300˚C. The thicknesses and index of refractions for the dielectrics were measured to be 130nm and 1.47 respectively for SiO_2, and 130nm and 1.82 respectively for SiN. Ohmic contacts were identical to that of GaN APDs mentioned on in the previous section.

First, the dark currents for an APD with SiN passivation and that with SiO_2 passivation were compared. As shown in Figure 4.4, a device with SiN showed a larger dark current compared to a device with SiO_2 passivation for reverse-bias < 35V. This is possibly because our SiN conditions are not yet optimized compared to SiO_2, and may contribute to a slightly higher sidewall leakage current for detectors at low-bias.

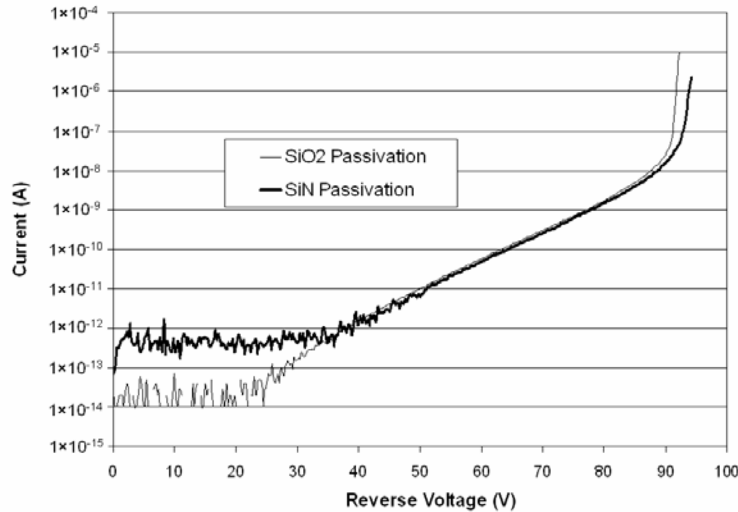

Figure 4.4: Dark current comparisons for APDs with SiO_2 and SiN passivations. The devices had a mesa diameter of 30 μm.

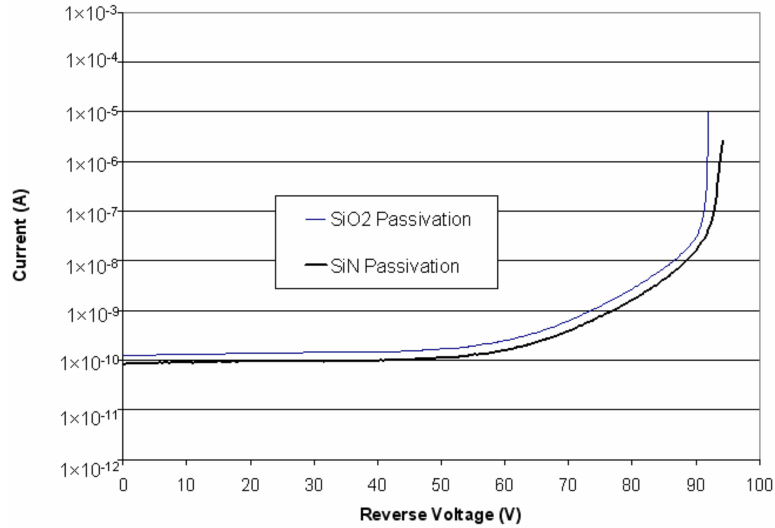

Figure 4.5: Photo current comparisons for APDs with SiO_2 and SiN passivations. The devices had a mesa diameter of 30 µm.

Figure 4.5 shows the photocurrent comparisons. A broadband UV source was used for photocurrent measurements. As shown, APD with SiO_2 passivation has a higher photocurrent compared to that with a SiN passivation. This is possibly due to the difference in index of refractions between the two dielectrics. For both devices passivated with different dielectrics, no micro-plasma or edge breakdown emission was visually observed.

Because the detector with SiO_2 passivation demonstrated superior performance for dark and photocurrents, SiO_2 dielectric passivation will used continuously for future detector device fabrications.

4.4 $Al_{0.05}Ga_{0.95}N$ Avalanche Photodiodes

To detect shorter wavelengths with high efficiency, the material needs to have a

wider bandgap. The $Al_xGa_{1-x}N$ epitaxial materials in this study were grown on low-dislocation-density ($<1\times10^7$ cm^{-2}) *n*-type bulk GaN substrates by metalorganic chemical vapor deposition (MOCVD) using a reactor system manufactured by Thomas Swan Scientific Equipment and equipped with a 7×2 close-coupled showerhead (CCS) growth chamber. The growth conditions are similar to that of GaN APDs, with the addition of trimethylaluminum (TMAl), and higher growth temperatures. Hydrogen (H_2) was used as the carrier gas and was mixed with ammonia (NH_3) as the Group V precursor and with EpiPure™ [29] trimethylgallium (TMGa) and trimethylaluminum (TMAl) as the Group III precursors. Silane (SiH_4) and bis-cyclopentadienyl magnesium (Cp_2Mg) were used as *n*-type and *p*-type dopant precursors, respectively. Prior to the epitaxial growth, the crystalline quality and the surface morphology of the bulk GaN substrate were characterized by X-ray diffraction (XRD), Nomarski optical microscopy, and atomic-force microscopy (AFM), respectively. AFM and XRD were also employed to determine the mole fraction of $Al_xGa_{1-x}N$ layers as well as the surface and crystalline quality of the epitaxial structures.

The epitaxial layer structure consists of an *n*-type $Al_{0.05}Ga_{0.95}N$:Si layer, followed by an unintentionally doped $Al_{0.05}Ga_{0.95}N$ drift region (0.25 μm, $n < 5\times10^{16}$ cm^{-3}), a *p*-type AlGaN:Mg^+ layer, and topped with *p*-type GaN:Mg^{++} (heavily Mg-doped) contact layer. The devices were fabricated into 30μm- and 50μm-diameter circular mesas by low-damage inductively coupled plasma (ICP) etching using a Cl_2/He carrier gas mixture. After mesa definition, an SiO_2 passivation layer was applied to the devices using plasma-enhanced chemical vapor deposition (PECVD). No attempt to taper the mesa side walls was made for device fabrication. Ti/Al/Ti/Au and Pd/Au Ohmic contacts were deposited

on *n*-layer and *p*-layer, respectively by an electron-beam evaporator system, and annealed at 600˚C in a N_2 ambient. The width of the dot-shaped *p*-contact metal is 12 μm. The complete device structure is schematically shown in Figure 4.6.

Improved crystalline and structural quality for $Al_xGa_{1-x}N$ (x~0.05) epitaxial layers was achieved by employing optimum growth parameters on low-dislocation-density ($<1\times10^7$ cm^{-2}) bulk GaN substrates, in order to minimize the defect density in the material. A graded layer from unintentionally doped GaN to $Al_xGa_{1-x}N$ (x = 0.05) was inserted as a strain management layer for a crack-free growth of AlGaN *p-i-n* structures on GaN substrates. Figure 4.7 shows the AFM images of the surface of $Al_{0.05}Ga_{0.95}N$ UV APD revealing atomic steps on the surface with no visible nano-pits. Root-mean square (RMS) roughness values are approximately 0.17 nm and 0.19 nm for 1×1 μm^2 scans and 5×5 μm^2 scans, respectively.

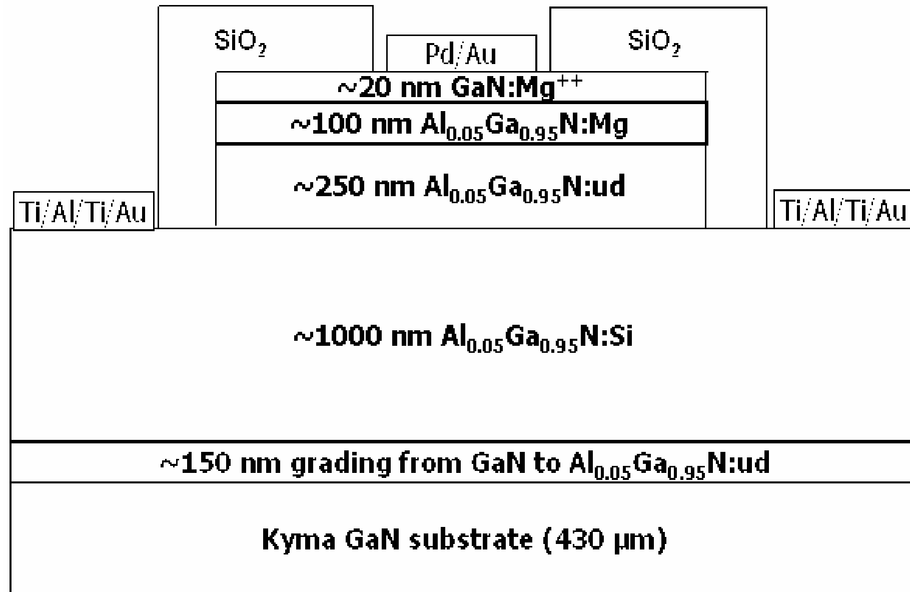

Figure 4.6: Schematic diagram of the $Al_{0.05}Ga_{0.95}N$ APD mesa-geometry device structure grown on a bulk GaN substrate.

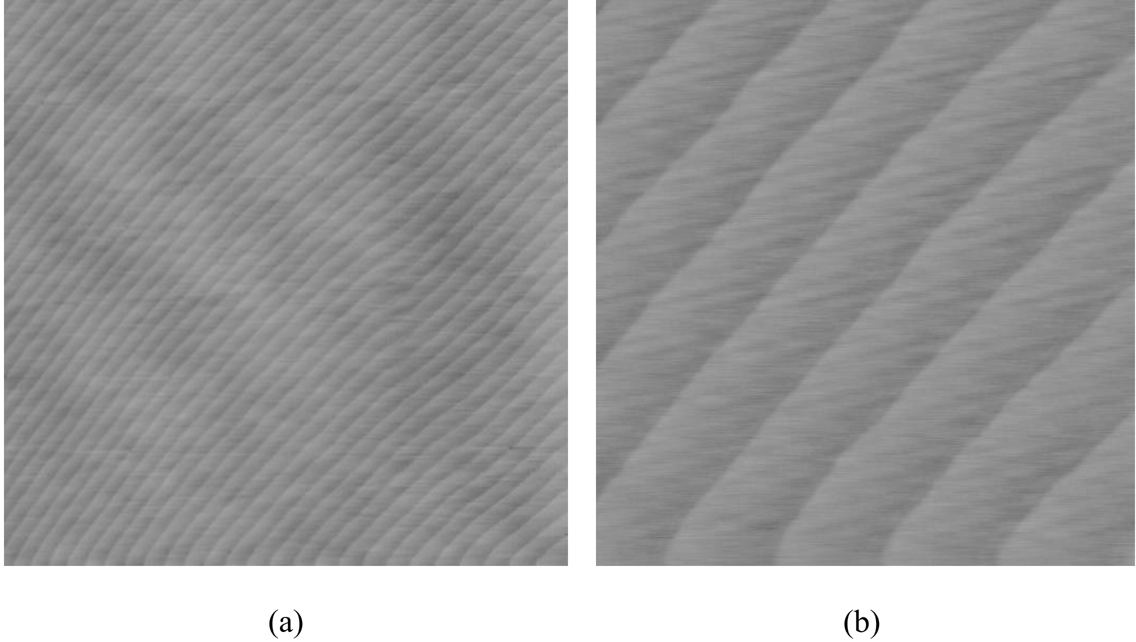

(a) (b)

Figure 4.7: AFM microscopic surface morphology of an $Al_{0.05}Ga_{0.95}N$ ultraviolet APD wafer grown on a bulk GaN substrate: (a) 5×5 μm^2 scan (b) 1×1 μm^2 scan with *z*-height scale of 10 nm.

The free carrier concentration and mobility in the *p*-type and *n*-type $Al_xGa_{1-x}N$ (x = ~ 0.05) layers were calibrated to be p=~5×10^{17} cm^{-3} with μ_h = ~8 cm^2/V·s and n=~3×10^{18} cm^{-3} with μ_e = ~200 cm^2/V·s, respectively, as determined by 300K Hall-effect measurements.

The reverse-bias voltage (up to -100V) *I-V* characteristics were measured using an Agilent HP4156C precision semiconductor parameter analyzer. Figure 4.8 shows a comparison of the photocurrent and dark-current characteristics at 300K for a 30 μm-diameter mesa AlGaN APD. No microplasmas or side-wall breakdown luminescence were visually observed. The photocurrent was obtained using a UV lamp-monochromator operating at a peak emission wavelength of ~254 nm. The avalanche gain (*M*) is taken as the difference between the reverse-biased photocurrent and dark current, divided by the difference between the low-bias photocurrent and low-bias dark

current. The photocurrent increases with bias. The reference unity gain photocurrent was taken at a reverse voltage of 70 V, assuming the worst case scenario. The avalanche gain reaches a maximum value of ~50 at a voltage of 86.75 V.

To our knowledge, this is the first demonstration of avalanche gain for AlGaN APDs. The avalanche gain is thought to be attributed to the low dislocation density of the substrates, low damage etching of the mesa, high quality dielectric passivation, and good crystalline quality of AlGaN epitaxial layers. Figure 4.9 shows a voltage-dependent photocurrent spectral response measured with a chopper-modulated optical signal and a lock-in amplifier.

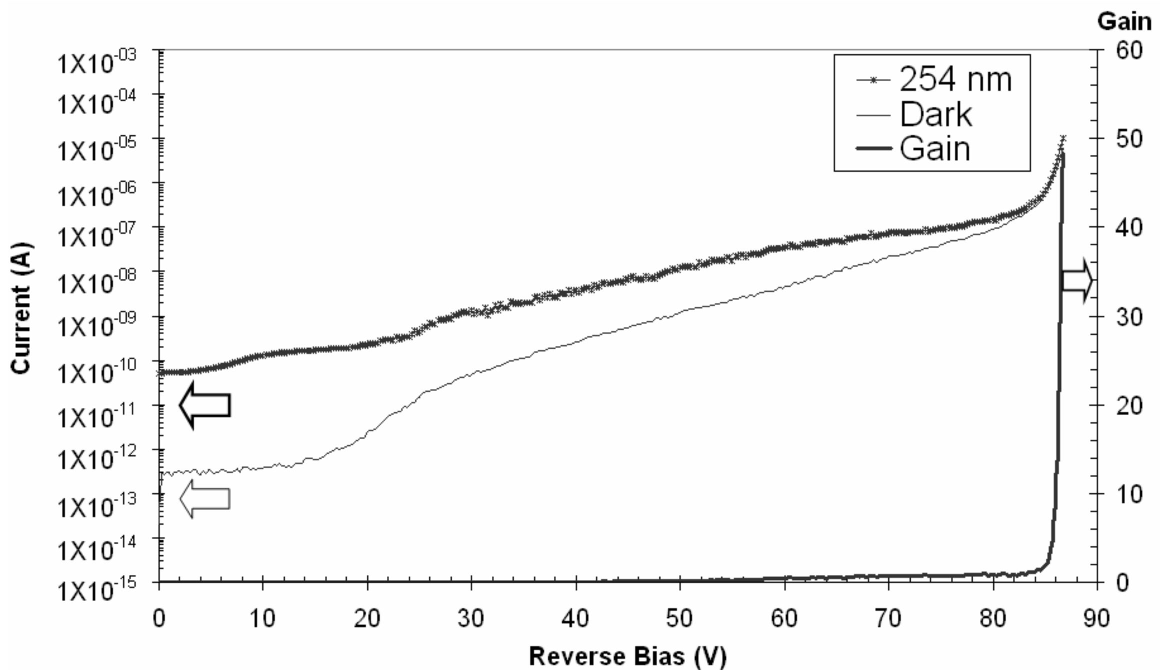

Figure 4.8: Reverse-bias *I-V* characteristics of an $Al_{0.05}Ga_{0.95}N$ ultraviolet avalanche photodiode having a mesa diameter of 30 μm. The illumination is provided by a ~254 nm source. The dark current, photocurrent, and avalanche gain (*M*) are plotted versus reverse bias voltage. The diode exhibits a maximum avalanche gain ~50 at a reverse bias of 86.75 V.

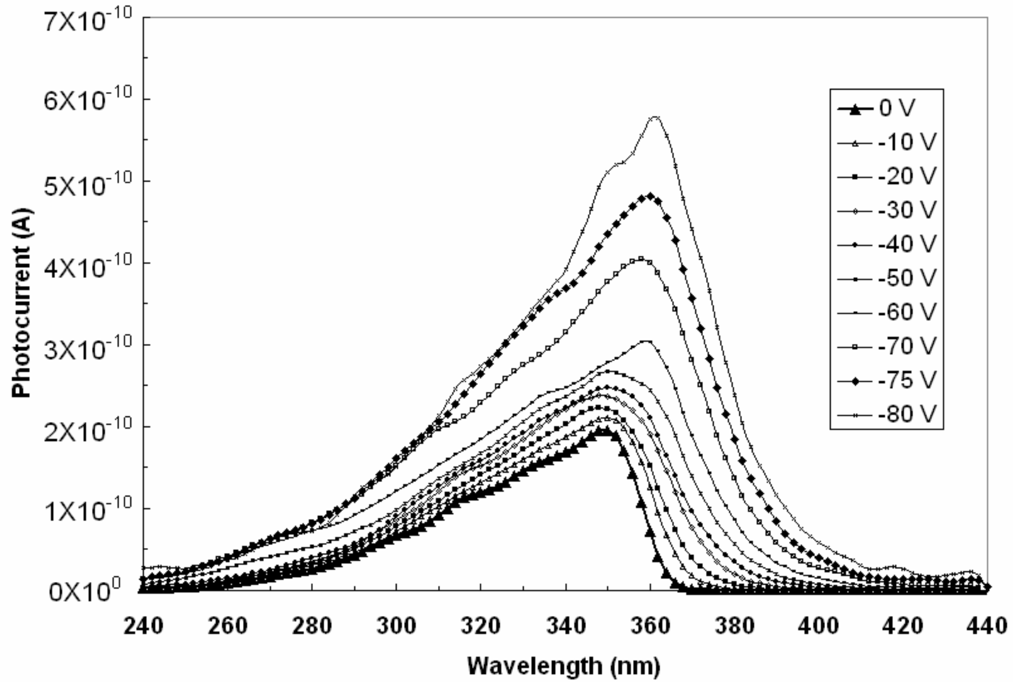

Figure 4.9: Spectral response for $Al_{0.05}Ga_{0.95}N$ ultraviolet avalanche photodiode having a mesa diameter of 30 µm. The voltage was varied from 0 to -80 V. The photocurrent starts to show significant increases from -60 Volt bias.

The zero-biased photocurrent showed a peak absorption at 350 nm (~3.54 eV) with an absorption edge at 364 nm (~3.4 eV). With the increase of reverse-bias, the absorption peak shifts slightly to near 370 nm due to the Franz-Keldysh effect. The response above shows that the short-wavelength cut-off wavelength for higher Aluminum composition (30%) AlGaN-based APD can be beyond 240 nm. With the increase of reverse bias, however, the absorption edge significantly extends into the blue band (~400 nm).

Since the UV light is illuminated from the top of the mesa, the photons are absorbed through both band-to-band transitions and acceptor-state absorption in the *p*-type layer. In addition to the band-to-band tunneling-assisted absorption in the depletion

region, the acceptor-to-conduction-band absorption in the *p*-GaN layer may be significant due to large number of unionized deep-level acceptor states. This situation is different from most lower-bandgap *p-i-n* diodes where shallow acceptors are presumably fully ionized. As a result, electrons at the un-ionized acceptor states will further induce significant red-shifting at the absorption edge due to the presence of linearly increased electric field.

4.5 Summary

In this chapter we have investigated the device performance of III-nitride based *p-i-n* avalanche photodiodes. To reduce the dislocation density of the material, the diodes were grown on free-standing GaN substrates. For GaN APDs grown on GaN substrates, dark current density was low until the devices operated deeply into avalanche. Optical gains greater than 3000 have been demonstrated. This is the first demonstration of true avalanche gain greater than 1000, for Nitride based APDs. We have also compared the device performance of APDs with SiO_2 and SiN passivations, and found out that detectors with SiO_2 passivations have shown lower dark currents. AlGaN APDs have also been grown and characterized. Avalanche breakdown has been achieved for AlGaN diodes with optical gain ~50. To our knowledge, this is the first demonstration of avalanche gain for AlGaN based *p-i-n* diodes.

CHAPTER 5

III-NITRIDE GREEN LIGHT EMITTING DIODES

5.1 Introduction

Recently, the development and commercial production of group III-nitrides have played a major role in high brightness light emitting diodes (LEDs). While great success has been reported in the development of LEDs in the blue and violet spectral region (λ=390~480nm), less success has been demonstrated in obtaining high quantum efficiency [31] and low forward voltages (V_f) for LEDs operating in the visible green spectral region.

The technological challenges lie not only in the difficulties to epitaxially grow high indium (In) composition $In_xGa_{1-x}N$ multiple-quantum-well (MQW) active region because of the contrasting thermodynamic properties of GaN and InN and their respective precursors, but also in the potential degradation of the multiple-quantum-well (MQW) active region during the relatively high-temperature growth of the *p*-layer. Especially in green LEDs, a beneficial effect of compositional inhomogeneity that is known to enhance the luminescence efficiency in violet and blue LEDs and laser diodes cannot play a role. Rather, the luminescence efficiency decreases by 1-2 orders of magnitude. It was reported that the degree of compositional fluctuations of the indium gallium nitride (InGaN) quantum wells also increases as the indium content increases. While the increase in the compositional fluctuations may enhance light emission near 410~430 nm, further increases in indium drive additional compositional fluctuations, resulting in significant disorder in the quantum well (QW) and a consequent reduction in the radiative

efficiency [32]. Also, group III-nitrides generate large piezoelectric fields because of the large piezoelectric constants, which lead to the quantum confined stark effect (QCSE) on optical properties [33]. Such an effect can be more significant in green LEDs than blue LEDs, since MQW is highly strained. These effects must be taken into consideration for the structural design of the LEDs.

5.2 Motivation for Using *p*-InGaN

First, we will compare the effects of "active region friendly" or low-temperature grown *p*-GaN and *p*-$In_{0.04}Ga_{0.96}N$ layers on the device performance of green LEDs. The low-temperature grown *p*-GaN and *p*-$In_{0.04}Ga_{0.96}N$ layers were used to reduce the optical degradation of the MQW active region, which occurs as a result of high-temperature annealing during the growth of the *p*-layer [36]. This degradation becomes even more significant for growth conditions in high-temperature hydrogen ambient. However, for LEDs with *p*-InGaN grown at low temperatures (840° C), only a slight decrease in photoluminescence (PL) intensity was observed because of its low temperature and nitrogen ambient growth, which are friendly conditions for the active region [36], [37]. This effect is shown in Figure 5.1. Notice that the PL intensity degradation is more significant for LEDs with *p*-GaN grown at 930° C compared to LEDs with *p*-$In_{0.04}Ga_{0.96}N$ grown at 840° C. Although *p*-GaN grown at 1040° C gives the most conductive GaN:Mg layer, such a growth condition cannot be employed in a green LED, as the high temperature growth of the subsequent *p*-layer can significantly degrade the active region, and emission characteristics of the diode becomes even weaker than that of the LED with *p*-GaN grown at 930° C [36], [37].

Besides its low temperature growth conditions, another motivation for using a high Indium composition p-$In_xGa_{1-x}N$ layer is such that it allows for higher hole concentration and conductivity compared with GaN:Mg because of its lower ionization activation energy [34]. We have compared the TLM I-V characteristics for LEDs with p-GaN and p-$In_{0.04}Ga_{0.96}N$ layers. The p-layer thickness was 70nm for both cases. As shown in Figure 5.2, the conductivity of p-$In_{0.04}Ga_{0.96}N$ layer is higher than conductivity of p-GaN layer.

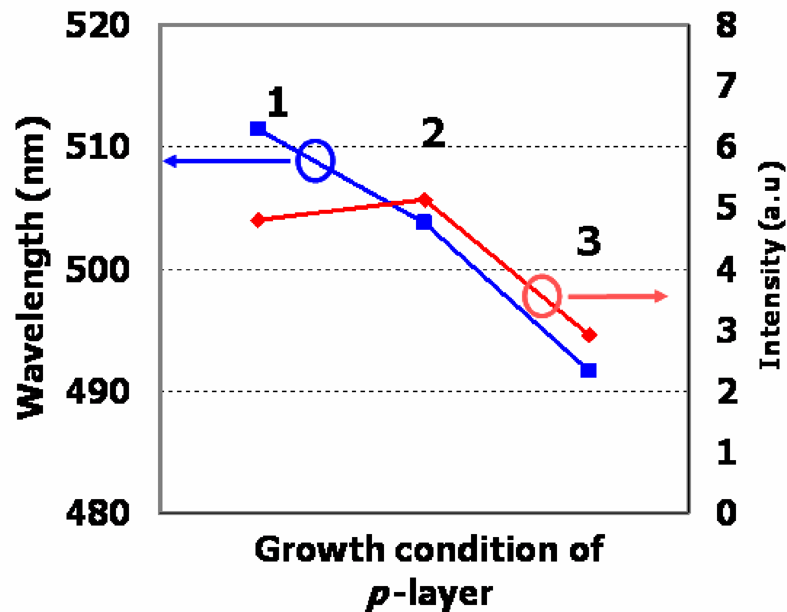

Figure 5.1: Influence of p-GaN and p-InGaN layer on the optical properties of green LEDs. (1) Without a p-layer, (2) With a p-InGaN layer grown at 840° C, (3) With a p-GaN layer grown at 930° C.

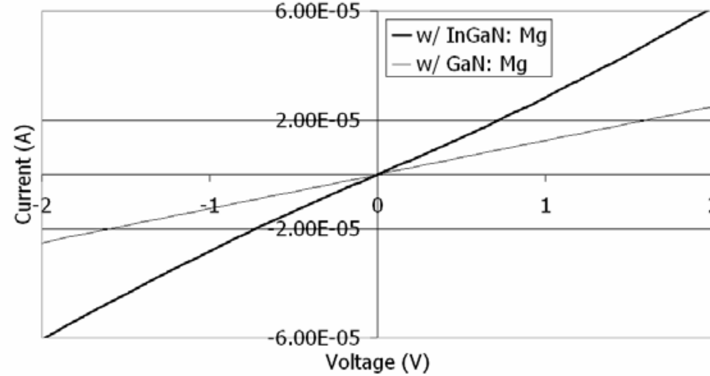

Figure 5.2: TLM *I-V* comparisons for LEDs with different *p*-layers. P-contacts consist of oxidized Ni/Au = 5 nm/5 nm. The TLM spacing was 14 um. P-layer thickness was 70 nm.

5.3 Comparison of LEDs Using *p*-InGaN and *p*-GaN Emitting at 518 nm

The epitaxial layers of *p*-type $In_{0.04}Ga_{0.96}N$:Mg and GaN:Mg, MQW active region, and LED structures were grown on *c*-axis (0001) sapphire substrates by metal-organic chemical vapor deposition (MOCVD) in a close-coupled showerhead reactor system [35]. Trimethyl-gallium (TMGa), trime-thylindium (TMIn), bis-cyclopentadienyl magnesium (Cp_2Mg), silane (SiH_4), and ammonia (NH_3) were used as precursors for Ga, In, Mg, Si, and N elements, respectively. Prior to the growth of LED structures, the growth condition for the active region friendly $In_{0.04}Ga_{0.96}N$:Mg and GaN:Mg layer grown at relatively low temperatures was calibrated to obtain the optimized electrical properties of the *p*-type layers. Detailed calibration and characterization for the *p*-type layers can be found in an earlier publication by Lee and Limb et al. [36]. Van der Pauw-geometry Hall-effect measurements carried out at room temperature revealed a hole concentration of ~2×10^{18} cm^{-3} with a mobility of ~7 cm^2/Vs for a *p*-$In_{0.04}Ga_{0.96}N$:Mg layer grown at 840° C in nitrogen ambient, while a hole concentration of ~5×10^{17} cm^{-3} with a mobility of

~7cm^2/Vs was achieved for a *p*-GaN:Mg layer grown at 930°C in hydrogen ambient. Although a higher hole concentration and mobility could be achieved for *p*-GaN:Mg layer grown at higher temperatures (1040°C), employing such a layer in an actual LED structure can significantly damage the optical properties of the LED, as determined from PL [37]. In the case of our LEDs with a high-temperature (1040°C) grown *p*-layer, the EL peak intensity was very low and therefore was not used here for comparison. Only the low-temperature grown *p*-layers mentioned above were used in the analysis.

An active region consisting of InGaN QW and a GaN quantum well barrier (QWB) was grown employing a two-temperature scheme. The QWs for the green LED structures in this study were grown at 740° C. Square-geometry devices with a 230 μm by 230 μm mesa were defined by inductively coupled plasma (ICP) etching using a silicon-dioxide (SiO_2) etch mask. Chlorine (Cl_2) and helium (He) were employed as carrier gases for ICP dry etching. Then, a wet chemical clean was used to mitigate the dry etch damage. After that, a buffered oxide etch (BOE) cleaning was used to etch away the SiO_2 etch mask. Ti/Al/Ti/Au electron-beam evaporation followed and was used to deposit *n*-type ohmic contacts. The *p*-layer ohmic contacts consisting of Ni/Au were deposited as the last step and then annealed in oxygen ambient to achieve linearity of contacts. The SEM images of the fully fabricated devices are shown in Figures 5.3 (a) and (b). For all the LEDs, the epitaxial structures, including the thickness of the QW and the QWB, and the interface quality between QW and QWB were characterized by X-ray diffraction (XRD). For photoluminescence (PL) measurements and PL mapping, the 266 nm line of Q switched laser was employed. XRD and electroluminescence (EL) were also used for analyzing the structural and optoelectronic properties of the LEDs.

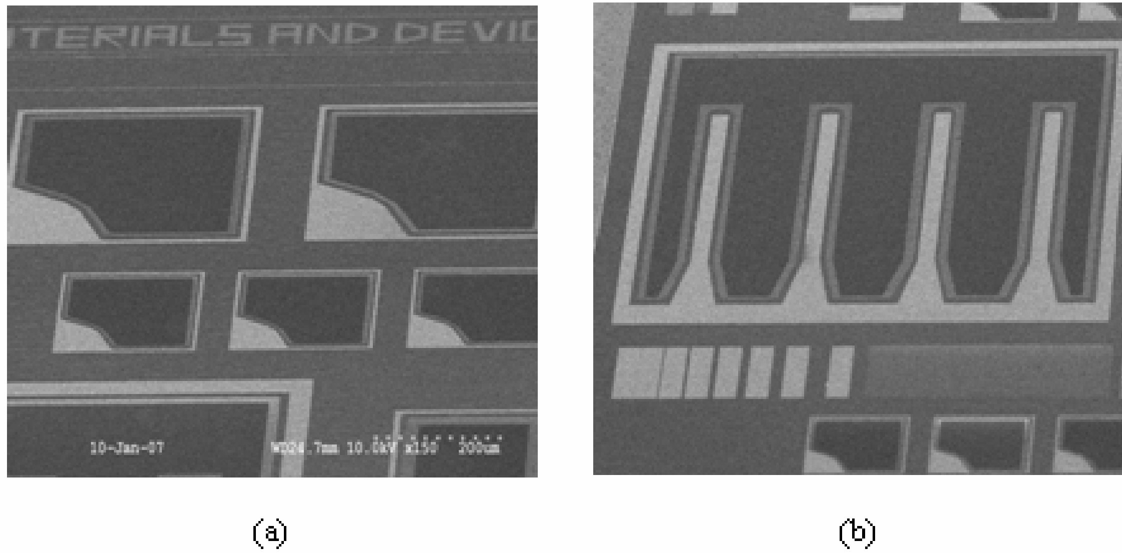

Figure 5.3: SEM Images of green LEDs (a) 230 μm by 230 μm and 350 μm by 350 μm devices, and (b) 1mm by 1mm devices.

PL and XRD analysis estimated that the MQW had a nominal well width of L_W = 2.5 nm, separated by barriers of nominal L_B = 8 nm. To study the effect of the *p*-type layer and respective growth condition on the active region of green LEDs, care was taken to have identical active regions for the green LED structures in this study. A description of the structures (a) and (b), employing *p*-type $In_{0.04}Ga_{0.96}N$:Mg and GaN:Mg, respectively, is shown in Figure 5.4

Figures 5.5 (a) and (b) show the room-temperature EL spectra for the LEDs with *p*-$In_{0.04}Ga_{0.96}N$ (structure (a) of Figure 5.4) and *p*-GaN (structure (b) of Figure 5.4) layers, respectively, at low current levels. For EL spectrum at high current levels, the peak is consistent with the MQW peak (510 nm ~ 520 nm) for both LEDs, which are close to the values measured from PL. The EL spectrum at high current levels will be discussed later, and is shown in Figure 5.6. However, for the low current levels, EL peak red shifts significantly from 565 nm for an injection current of 3 mA; 560 nm at 5 mA; 545 nm at

10 mA; 525 nm at 15 mA; and 520 nm at 20 mA for the LED with a p-$In_{0.04}Ga_{0.96}N$ layer. This is shown in Figure 5.5 (a). Such a significant red shift at low current levels cannot be observed in an LED with a p-GaN layer (Figure 5.5 (b)).

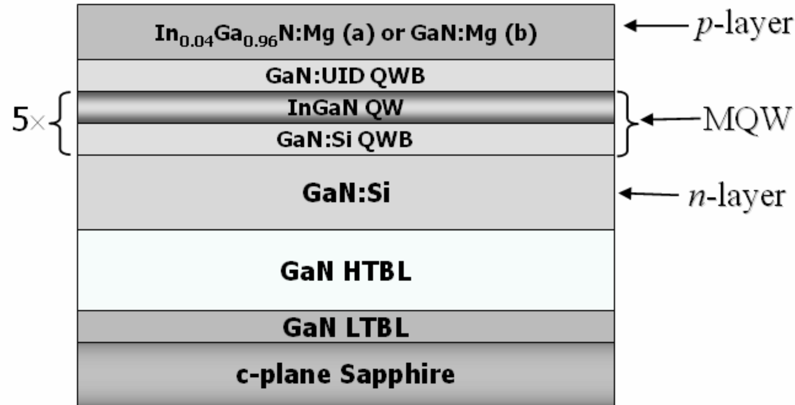

Figure 5.4: Schematic structures of the green LEDs in this study with (a) p-$In_{0.04}Ga_{0.96}N$: Mg grown at 840°C, and (b) p-GaN:Mg layer grown at 930°C.

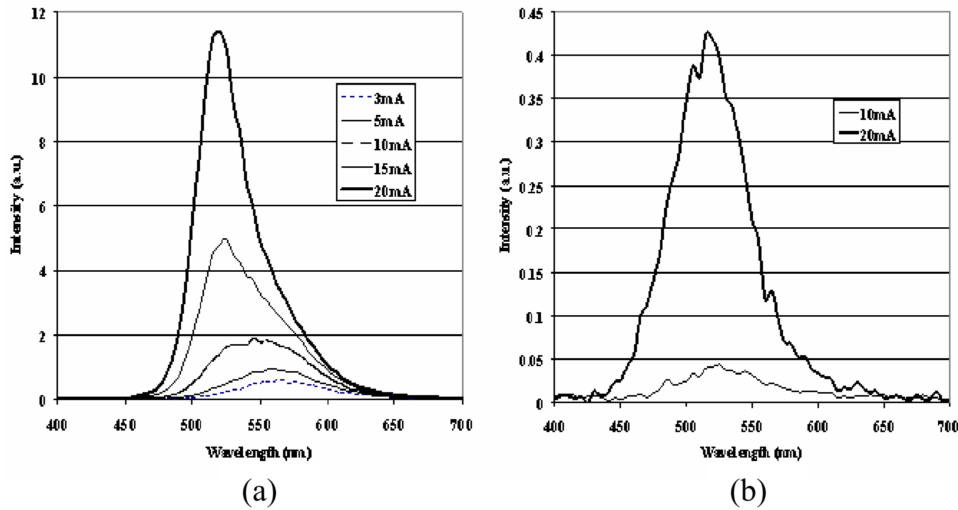

Figure 5.5: The room temperature EL spectra of green LEDs at low current levels: (a) with p-$In_{0.04}Ga_{0.96}N$:Mg layer; (b) with p-GaN:Mg layer. Note that the EL peak changes significantly for LED with p-$In_{0.04}Ga_{0.96}N$:Mg layer at all current levels, while virtually no change is shown for LED with p-GaN:Mg layer.

For an LED with a *p*-GaN layer, the EL peak is at 525 nm for 10 mA of current and 520 nm for 20 mA, which show only small deviations from the MQW peak (compared with PL data) for low current levels.

We believe this significant red shift at low current levels for LEDs with the *p*-$In_{0.04}Ga_{0.96}N$ layer can be attributed to lowering the energy eigenvalues in the MQW as a result of the abrupt heterojunction between *p*-$In_{0.04}Ga_{0.96}N$ and GaN barrier layer below. Such a long wavelength shift may not be due to the formation of V-defects [38], since we observe the quantum confined start effect (QCSE) at low bias currents. Also, this effect is not shown for the LED with a *p*-GaN layer since there is no polarization between *p*-GaN and the quantum well (QW) barrier just below that would modify the energy levels of the MQWs. Although such a polarization resulting from the InGaN layer can influence the electrostatics of the remaining quantum wells (QWs), that influence should be very small, especially since all the barriers for the QWs are doped with silicon (for the purpose of minimizing quantum confined stark effect) and should be somewhat pinned close to the Fermi level.

However, it still causes the energy levels to red shift relative to the LED with a *p*-GaN layer. For low current levels (bias voltages below 2.8 Volts), most of the carriers injected from the terminals have shown recombination at this lower energy level. The polarization-induced recombination will also tend to blue shift (from 565 nm to 545 nm as current varies from 3 mA to 10 mA) until the carriers are able to overcome this recombination. Hence, up to current levels of 10 mA and below, we only see an EL peak with significant red shift because of the polarization between InGaN:Mg and GaN, as shown in Figure 5.5 (a) at wavelengths between 565 nm to 545 nm. Although the

calculated first energy eigenstate for electrons is slightly lower for the LED with InGaN:Mg compared to the LED with GaN:Mg, it still doesn't explain clearly why the polarization-induced recombination shifts to much longer wavelengths at low currents. Possibly, additional energy eigenstates have been formed due to this polarization. Also, the intensity is very low compared to MQW-induced recombination, to be shown later. Once the current exceeds 15 mA, the holes start to actively overcome this polarization-induced recombination and recombine in the MQWs, where a more dominant EL peak starts to show up at ~520 nm. This is shown in Figure 5.5 (a) for current levels of 15 mA and 20 mA. At even higher current levels (20 mA and higher), only the MQW peak shows (Figure 5.6 (a)), meaning a large number of carriers are now recombining in the quantum wells. However, once this happens, the EL intensity of the LED with the *p*-$In_{0.04}Ga_{0.96}N$ layer is much higher than that with the *p*-GaN layer [39], as shown in Figure 5.6. This is possibly due to enhanced hole injection into the active region with superior *p*-type material properties of *p*-InGaN compared to *p*-GaN.

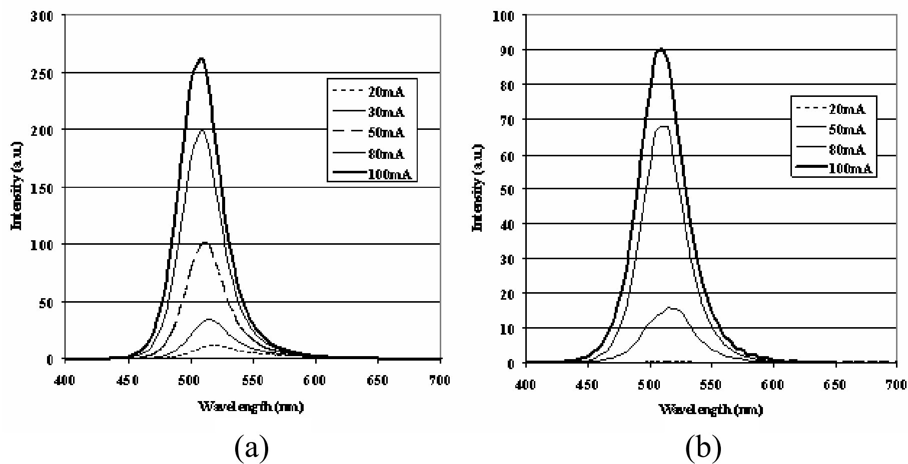

Figure 5.6: The room temperature EL spectra of green LEDs at high current levels: (a) with *p*-$In_{0.04}Ga_{0.96}N$:Mg layer; (b) with *p*-GaN:Mg layer. Note that the EL peak does not change much once the current level exceeds 20 mA for both cases.

Also, a less severe thermal degradation of MQW for LEDs with a *p*-InGaN layer grown at lower temperature could be another reason for the improvement in EL intensity compared to LEDs with a *p*-GaN layer. Figure 5.7 shows current-voltage characteristics of green LEDs with different *p*-layers.

The LEDs with *p*-GaN and *p*-InGaN both show low turn-on voltages, with the latter case being slightly higher, while forward voltages (at a drive current of 20 mA) were 3.1 and 3.2 V respectively, indicating that the LED devices show very low resistivity even for device dimensions of only 230 x 230 μm^2. We believe that the low turn-on voltages are partially attributed to the doping of the QWBs, as well as high quality of the bulk material. The diode series resistances are ~ 24.7 Ω for LEDs with *p*-GaN, and ~ 18.5 Ω for LEDs with *p*-InGaN.

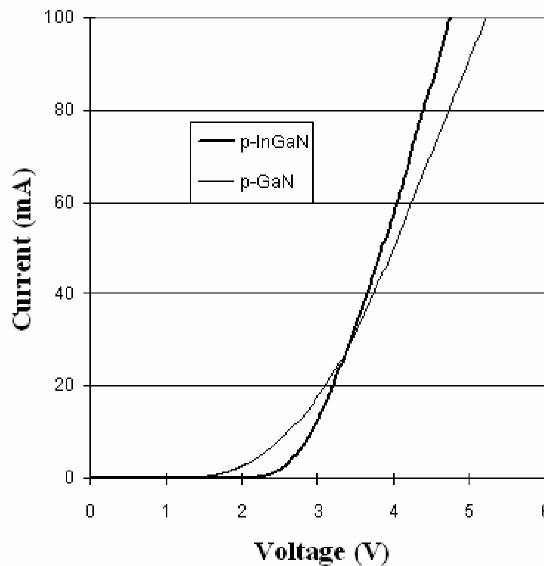

Figure 5.7: Current-voltage characteristics of green LEDs with different *p*-layers at room temperature. The LED with *p*-$In_{0.04}Ga_{0.96}N$ layer show slightly higher V_f of ~3.2 V at 20 mA, while LED with *p*-GaN layer show a V_f of ~3.1 V. However, the LED with *p*-$In_{0.04}Ga_{0.96}N$ layer clearly shows lower diode series resistance. LED device dimensions are 230 x 230 μm^2.

Clearly, the LEDs with *p*-InGaN layers show a higher turn on voltage and forward voltage. This is possibly due to an additional potential barrier that exists at the abrupt heterojunction between the *p*-InGaN layer and the upper GaN QW barrier just below the *p*-layer, which produces an additional barrier to current flow. Figure 5.8 shows the simulated band-diagram of LEDs employing different *p*-layers, drawn together. It shows an additional potential barrier to carrier flow, for LED with *p*-InGaN layer. However, the higher hole concentration and lower resistivity for the LEDs with *p*-InGaN layers could provide a lower diode series resistance and better current spreading compared to the LEDs with *p*-GaN layers at higher currents.

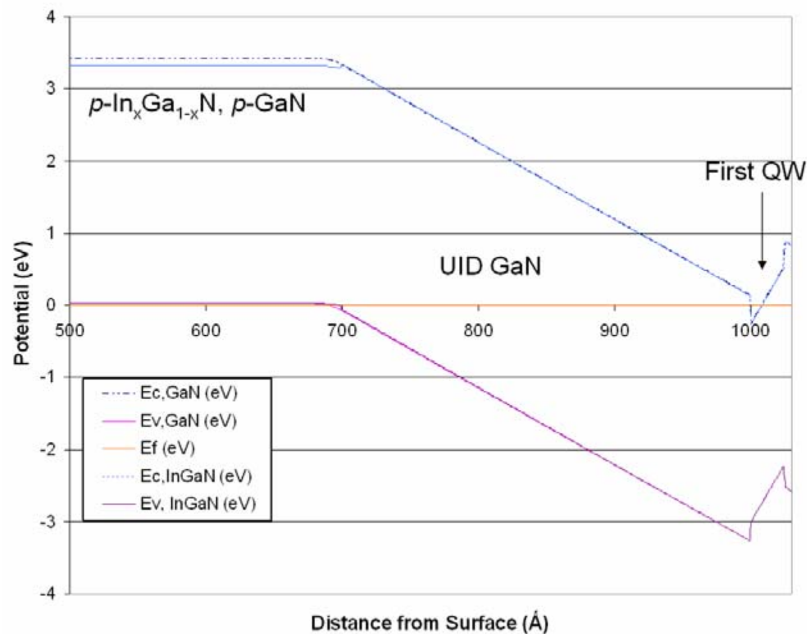

Figure 5.8: Simulated band-diagram of LEDs with *p*-$In_{0.04}Ga_{0.96}N$ and *p*-GaN layers drawn together: *p*-layers, UID GaN barrier, and first QW are drawn. For LED with a *p*-$In_{0.04}Ga_{0.96}N$ layer, there is an abrupt heterojunction barrier between the *p*-$In_{0.04}Ga_{0.96}N$ and UID GaN layers.

5.4 Effect of Silicon Doping of Quantum Well Barriers on LED Performance.

Previously, LEDs with *p*-type InGaN has shown improved light emission characteristics compared to LEDs with *p*-type GaN. While using the *p*-$In_{0.04}Ga_{0.96}N$ layer as the *p*-layer for the LEDs, we have grown and characterized several green LED structures to study the effect of Si doping in the QWB on the electrical and optical properties of the device as well as the band structure of the active region. Si doping of the QWB can have following effects on active region: (1) the screening of strain induced piezoelectric field; (2) the screening/enhancement of localization effect (potential fluctuation); (3) the improvement/degradation of material quality of MQW depending on doping level; and (4) the modification of the carrier transport.

We have studied the electrical properties and optical properties of green LED structures depending on Si doping scheme in the QWB. Si was varied from unintentionally doped (*uid*; Si flow rate = 0 sccm)) to Si~8×10^{18} cm^{-3} (Si flow rate = 8 sccm). Figure 5.9 shows the effect on Si doping in the QWB on the electrical characteristics of the LEDs. Clearly, as the Si doping increases, the forward voltage decreases. For Si dopings of 0 sccm, 4 sccm and 8 sccm, the forward voltages of the LEDs (at 20 mA), are 3.85 V, 3.65 V, and 3.48 V respectively. This is possibly because, as the Si doping in the barrier increases, the conduction band barrier energy levels become closely pinned to the Fermi level. This should reduce the potential barriers for carrier transport, and therefore reduce forward voltages. Figure 5.10 (a), (b), (c) shows the electroluminescence (EL) properties of the diodes with different Si dopings in the barriers. Clearly EL peak intensity continuously decreases, as Si doping in QWB increases. As Si doping in QWB increases, the extra charge will have an additional effect

of screening the piezoelectric field, flattening the conduction/valence band potential in the well.

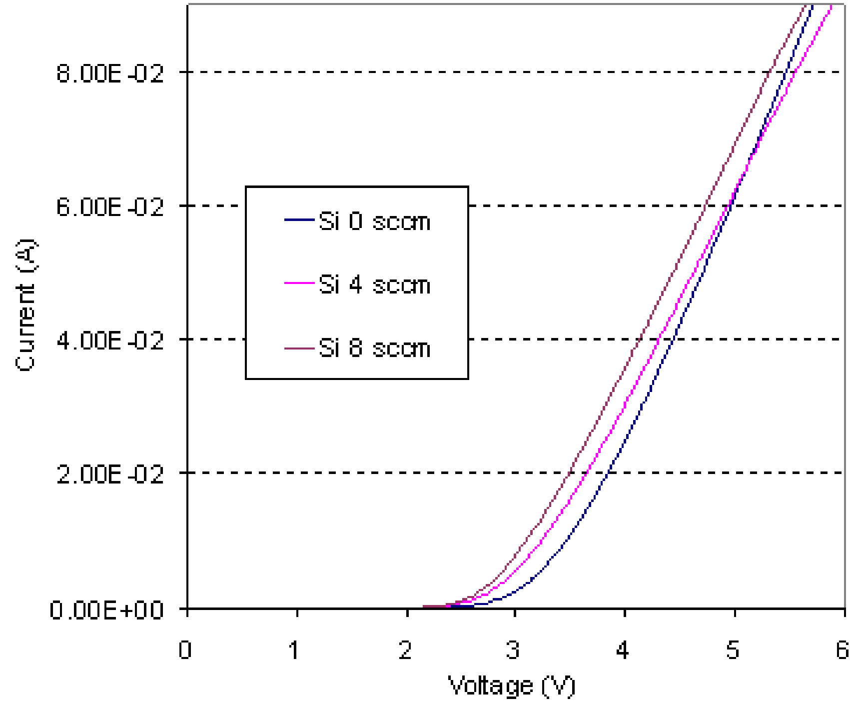

Figure 5.9: Current-voltage characteristics of green LEDs with different Si-doping in the QWB. The Si doping was varied from Si = 0 sccm, Si = 4 sccm, and Si = 8 sccm in GaN QWB. V_f =3.85 V, 3.65 V, and 3.48 V at 20 mA, for Si = 0 sccm, 4 sccm, and 8 sccm respectively.

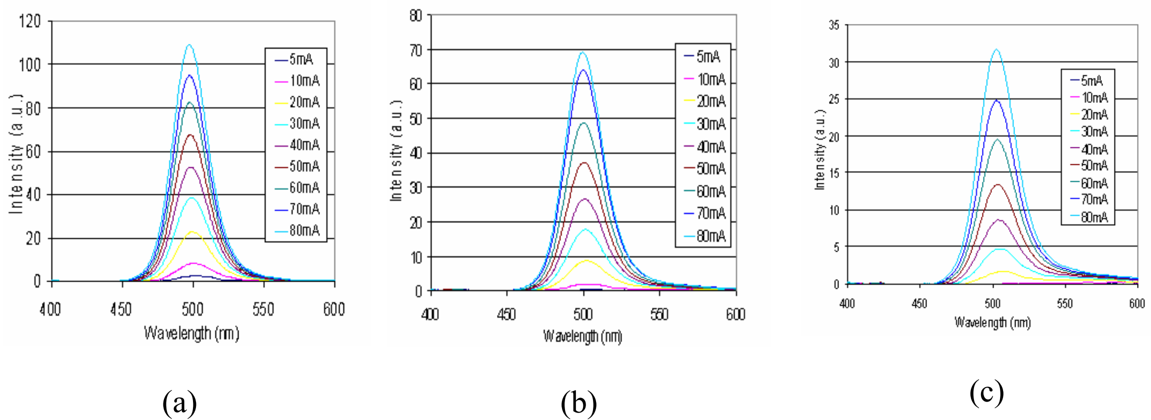

Figure 5.10: Electroluminescence characteristics of the green LEDs having different Si doping level in GaN QWB: (a) Si = 0 sccm (unintentionally doped), (b) Si = 4 sccm, and (c) Si = 8 sccm.

This however, could reduce the efficiency for trapping the carriers in the quantum well, reducing the efficiency for carrier recombination. Other than this explanation, such observations may suggest followings: (1) too much Si doping might cause the degradation of MQW; and (2) too much Si doping might cause the *p-n* junction shift.

5.5 Green LEDs Emitting at 525nm and Longer Wavelengths

So far, the green LEDs showed light emission at wavelengths below 520 nm at 20mA of drive current. For diodes with longer wavelength emissions, more indium needs to be incorporated into the active region. This requires a lower temperature growth for higher indium incorporation. Another important point is that LEDs with no intentional doping in the QWB showed the brightest emission characteristics. Therefore, we have employed LEDs with no intentional doping in the well barriers for longer wavelength emitting diodes. The structure for LEDs emitting at ~525 nm and longer wavelengths at 20 mA of drive current is shown in Figure 5.11. Figure 5.12 (a) shows the EL characteristics of an LED emitting at ~526 nm for a drive current of 20 mA. Figure 5.12 (b) shows the current voltage characteristics of the LED for device dimensions of 350 μm by 350 μm. The forward voltage is 3.66V at 20 mA, and the diode series resistance is calculated to be 17.27 Ω. The peak internal quantum efficiency was extracted to be 25% for this sample. Figure 5.13 shows the structure for LEDs emitting at ~545 nm and longer wavelengths. Indium incorporation of more than 30% is required for longer wavelength emissions. Figure 5.14 (a) shows the EL characteristics of an LED emitting at ~545 nm for a drive current of 20 mA. As shown in Figure 5.14

(b), the forward voltage is only 3.58 V at 20 mA, and diode series resistance is only 16.5 Ω for device dimensions of 350 µm by 350 µm.

$In_{0.04}GaN$: Mg contact layer (20 nm)
$In_{0.04}Ga_{0.96}N$: Mg (100 nm)
GaN: nid (9.0 nm)
$In_{0.28}Ga_{0.72}N$ (2.5 nm) x5
GaN: nid (9.0 nm) x5
GaN: Si (120 nm)
GaN: Si- (300 nm)
GaN: Si (1000 nm)
GaN: Si (500 nm)
Al_2O_3

Figure 5.11: The structure for green LEDs emitting at ~526 nm. The Indium composition was investigated by Xray and PL measurements.

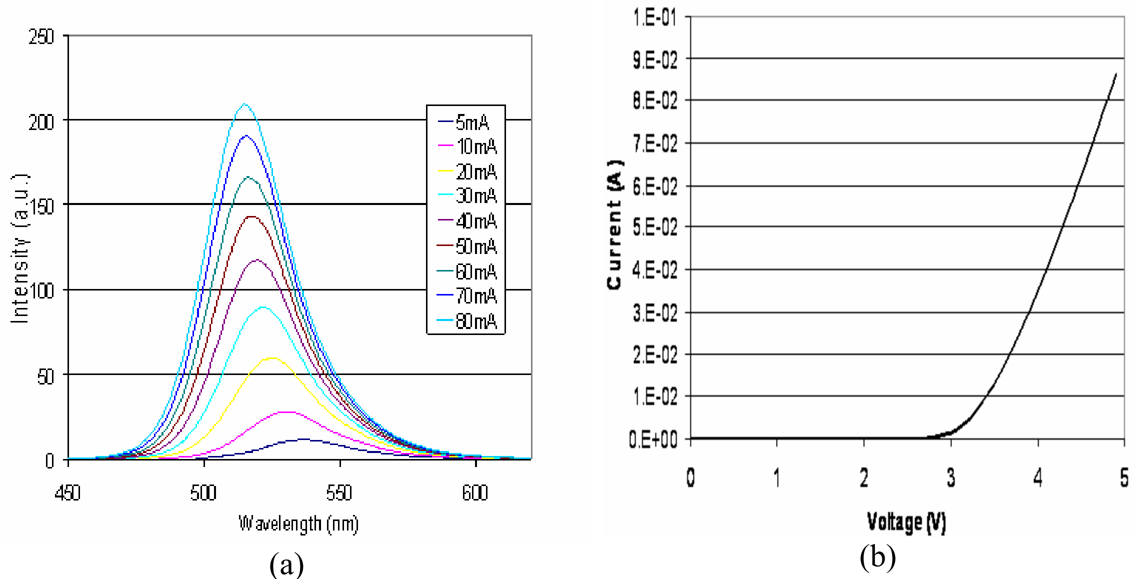

(a) (b)

Figure 5.12: (a) EL characteristics of green LEDs emitting at ~526 nm at 20 mA (b) *I-V* characteristics of the diode showing a forward voltage of 3.66 V at 20 mA. The device dimensions are 350 × 350 µm^2.

The peak internal quantum efficiency was extracted to be 13% for LEDs emitting at 545 nm.

$In_{0.04}GaN$: Mg contact layer (20 nm)
$In_{0.04}Ga_{0.96}N$: Mg (100 nm)
GaN: nid (9.0 nm)
$In_{0.32}Ga_{0.68}N$ (2.5 nm) x5
GaN: nid (9.0 nm) x5
GaN: Si (120 nm)
GaN: Si- (300 nm)
GaN: Si (1000 nm)
GaN: Si (500 nm)
Al_2O_3

Figure 5.13: The structure for green LEDs emitting at ~545 nm. Higher Indium incorporation in the active region is necessary for longer wavelength emissions.

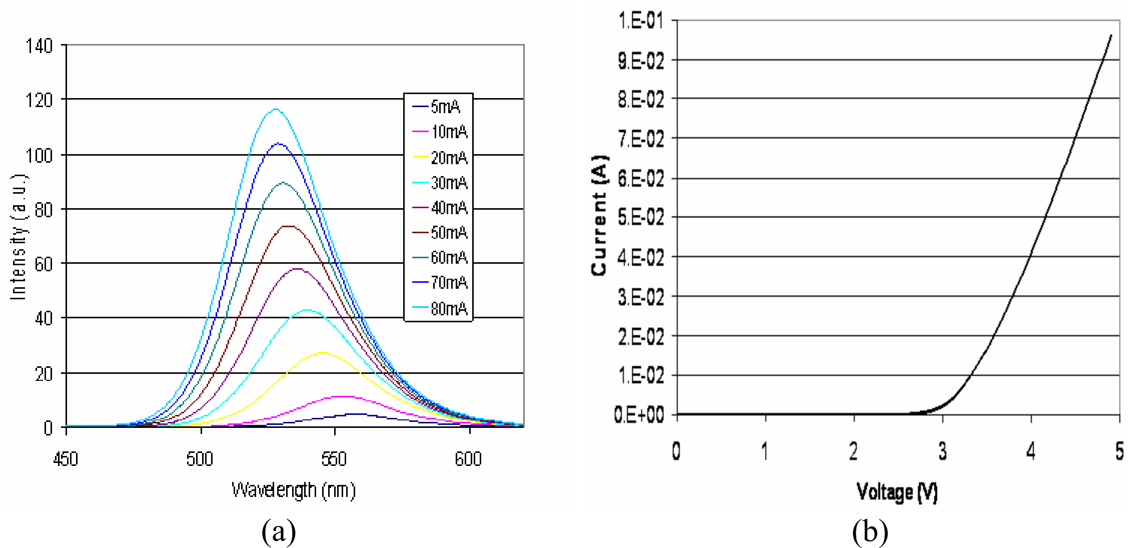

Figure 5.14: (a) EL characteristics of green LEDs emitting at ~545 nm at 20 mA (b) *I-V* characteristics of the diode showing a forward voltage of 3.58 V at 20 mA. The device dimensions are 350 × 350 μm^2.

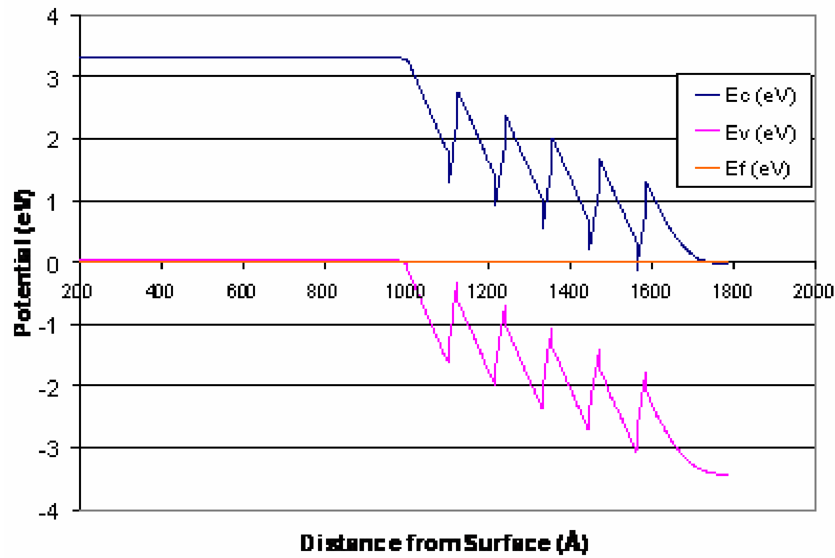

Figure 5.15: Simulated band-diagram of an LED emitting at green and longer wavelengths, using a *p*-$In_{0.04}Ga_{0.96}N$ layer and an active region with an indium composition of 30% in the quantum wells.

Figure 5.15 shows the simulated band-diagram of an LED emitting at green and longer wavelengths, assuming an indium composition of 30% in the quantum wells. This figure shows that the quantum wells are highly strained.

One of the reasons for having low forward voltages and low diode series resistances for the LEDs is because of low resistance Ohmic contacts to the LEDs using a transparent *p*-metal contact (Ni/Au =5nm/5nm). The TLM characteristics for the LED *p*-contacts are shown in Figure 5.16. The contacts were annealed in an oxygen environment to achieve linearity of contacts. The specific contact resistivity was measured and calculated to be comparable to that of Pd/Au contacts.

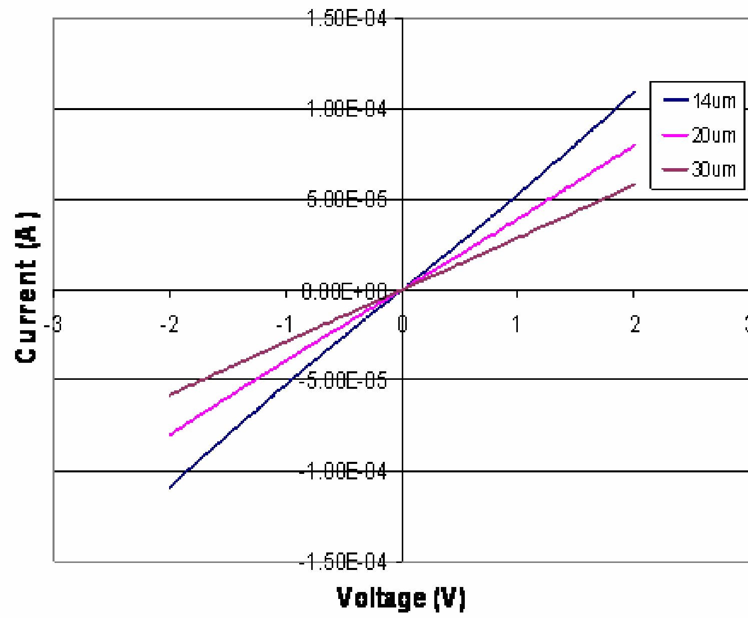

Figure 5.16: Transparent *p*-contact characteristics of an LED emitting at green and longer wavelengths, with a *p*-$In_{0.04}Ga_{0.96}N$ layer. Ni/Au = 5nm/5nm was annealed at 600 ^{o}C in an oxygen ambient to achieve linear contact characteristics.

5.6 Summary

In this chapter, we have investigated visible light emitting diodes with emission spectrum from green to longer wavelengths, grown by MOCVD.

First, we have compared the effects of *p*-GaN and *p*-InGaN on the electrical and optical properties of the diodes. We have shown that LEDs with *p*-InGaN have higher emission intensities compared to LEDs with *p*-GaN. There are 2 possible reasons for this: (1) InGaN:Mg is active region friendly, grown at lower temperatures. (2) *p*-type InGaN is more conductive compared to *p*-type GaN, improving hole-injection for LEDs employing *p*-InGaN compared to LEDs employing *p*-GaN.

Second, we have investigated the effects of Si-doping in the QWB on the electrical and optical properties of the diodes. We have shown that brightest emission is achieved for diodes with undoped (UID) QWB, although it exhibits the largest forward voltage. With this analysis, undoped QWB LED structures for longer wavelength LEDs were used.

Finally, we have grown, fabricated and characterized LEDs emitting at green (~526 nm) and longer wavelengths (~545 nm) employing *p*-type InGaN layers, without intentional doping in the QWBs. The peak internal quantum efficiencies were extracted to be 25% and 13% respectively, for these samples. For LEDs emitting at ~526 nm, a forward voltage below 3.7 V at 20 mA and a diode series resistance of 17.3 Ω was achieved, for device dimensions of 350 × 350 μm^2. For LEDs emitting at ~545 nm at 20 mA of drive current, a forward voltage below 3.6 V was achieved for device dimensions of 350 µm by 350 µm, with a diode series resistance of only 16.5 **Ω.** To our knowledge, this is the first demonstration of III-nitride based green LEDs employing *p*-InGaN layers.

CHAPTER 6

III-NITRIDE PIN RECTIFIERS

6.1 III-Nitride *p-i-n* Rectifiers as Power Devices

The primary advantage of employing *p-i-n* rectifiers as power devices is to benefit from the low resistance during the "On-state" operation of a rectifier [40]. Thus, the device can sustain a high current density under forward bias with low power losses, which is one of the critical aspects for many high-power device applications. Also, the large breakdown-field of GaN, make *p-i-n* rectifiers suitable as power devices. These devices are expected to provide a new paradigm for power switching applications and to enable a new generation of high-power and high-temperature switching electronics, leading to higher efficiency, lower cost, and lower weight space-based systems.

6.2 Vertical Mesa Rectifier Structure on SiC Substrate

GaN-based materials are usually grown on either sapphire substrates or silicon-carbide (SiC) substrates. The growth on the SiC substrates has advantages over the growth on sapphire substrates because it enables a reduced degree of lattice mismatch. Hence, a lower-defect density in the epitaxial GaN-based layers and a higher thermal conductivity of the substrate (thermal conductivity, $\kappa_{(6H\text{-}SiC)} = 3.3$ W/cm·K and $\kappa_{(sapphire)} = 0.4$ W/cm·K). This enables better thermal management for the device operation of the rectifiers. The advances in SiC substrate manufacturing technologies over the past decade allowed them to be used in a variety of high-power electronic devices [41]. For the growth of GaN on a SiC substrate, aluminum nitride (AlN) grown at a high

temperature has been shown to be a suitable buffer layer because of its relatively small *a*-axis lattice mismatch of approximately 1% [42]. Device fabrication and characterization of GaN *p*-*i*-*n* rectifiers grown on SiC substrates with a conventional AlN buffer layer using the deep dry etching is first studied.

6.2.1 Vertical Mesa *p-i-n* Rectifiers on SiC Substrates

First, *p*-*i*-*n* rectifiers using a mesa structure grown on a SiC substrate was fabricated. GaN epitaxial materials used in this study were grown on 6H *n*-type SiC substrates by metal-organic chemical vapor deposition (MOCVD) using a reactor system (manufactured by Thomas Swan Scientific Equipments) equipped with close-coupled showerhead (CCS) growth technology. Hydrogen (H_2) was used as the carrier gas mixed with ammonia (NH_3) as a hydride precursor and with EpiPure^{TM} trimethylgallium (TMGa) and trimethylaluminum (TMAl) as alkyl precursors. Silane (SiH_4) and bis-cyclopentadienyl magnesium (Cp_2Mg) were used as *n*- and *p*-type dopant precursors, respectively. Figures 6.1 and 6.2 illustrate the structure and SEM image of the GaN *p*-*i*-*n* rectifier devices studied in this work.

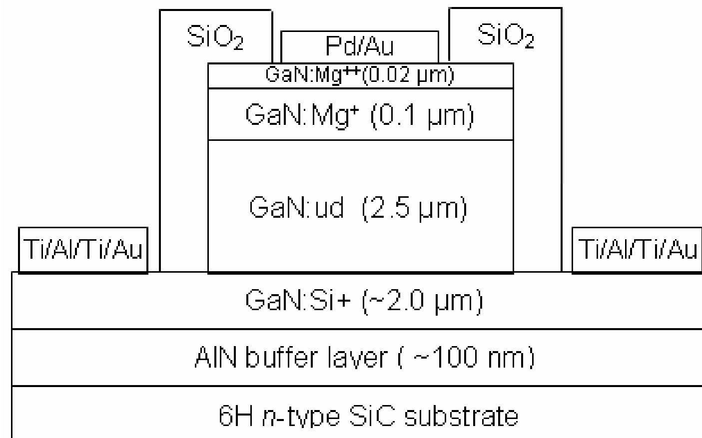

Figure 6.1: A schematic diagram of the *p*-*i*-*n* GaN rectifier structure.

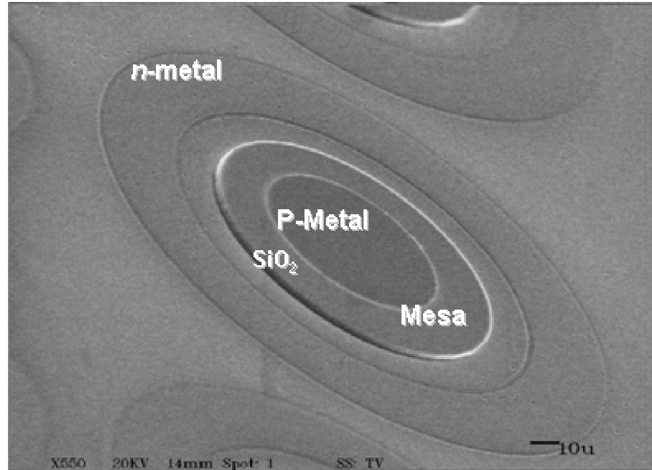

Figure 6.2: SEM image of the fabricated device with mesa dimension of 80 μm.

The carrier concentrations for the *p*-type and *n*-type regions were estimated to be p~1x10^{18} and n~5x10^{18} cm^{-3} from the Hall-effect measurements on thicker layers grown under similar conditions. The intrinsic doping level of unintentionally doped *i*-GaN was assumed to be n~5×10^{16} cm^{-3}.

Photolithography and inductive coupled plasma (ICP) etching with Cl_2 and He etching species were employed to define the mesa structure. Then, a wet-chemical cleaning step was used to remove the dry-etch damage. Immediately after the wet-cleaning step, an SiO_2 passivation layer was deposited by a plasma-enhanced chemical vapor deposition (PECVD). An electron-beam evaporator was used to deposit the *n*-type ohmic contacts consisting of Ti/Al/Ti/Au (200Å/800Å/200Å/700Å) and the *p*-type ohmic contacts of Pd/Au (200Å/800Å). The rectifier devices had a mesa diameter of 80 μm with a metal contact diameter of 60 μm. The current density is based on the mesa area. The best devices exhibited a blocking voltage as large as ~ -500 V at a reverse-current density of 1 A/cm^2 (Figure 6.3), and a forward voltage drop of only ~4.6 V at a forward-

current density of ~100 A/cm^2. It also had an on-resistance of 2.3 mΩ·cm^2 (Figure 6.4), yielding a figure-of-merit value of $(V_{RB})^2/R_{ON}$ = 108 MW/cm^2[43].

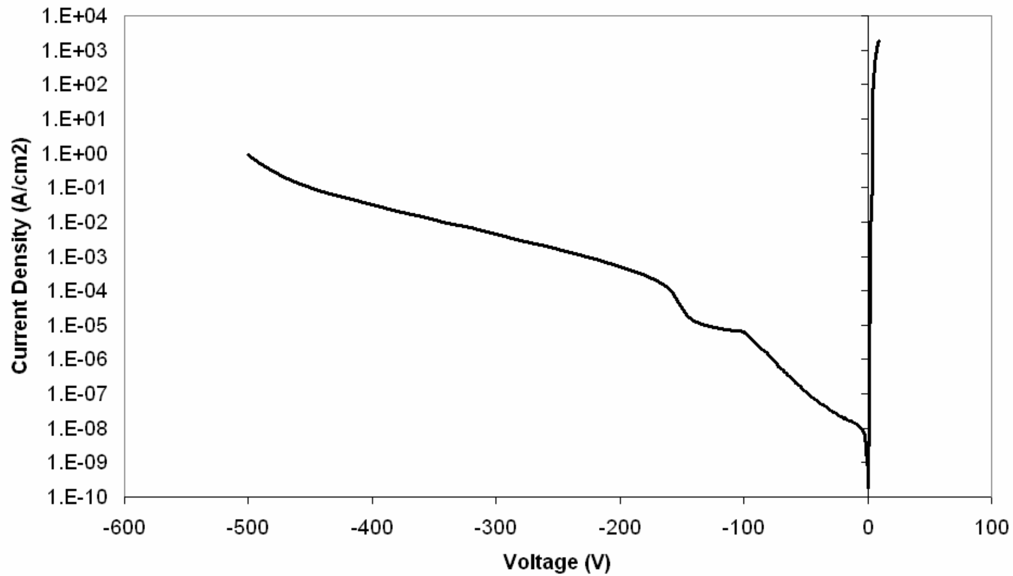

Figure 6.3: Current-voltage characteristics of a mesa etched GaN *p*-*i*-*n* rectifier in log-scale. The mesa diameter is 80 µm.

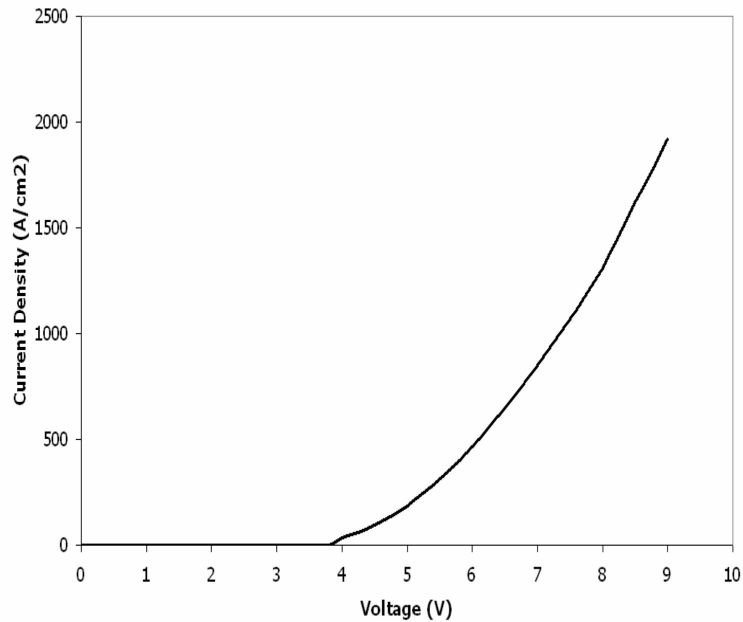

Figure 6.4: Forward current-voltage characteristics of a mesa etched GaN *p*-*i*-*n* rectifier. The mesa diameter is 80 µm. The maximum current density exceeds 1900 A/cm^2.

6.3 Vertical Mesa *p-i-n* Rectifiers on Freestanding GaN Substrates

GaN *p-i-n* rectifiers were grown on Lumilog GaN substrates. The growth on GaN substrates eliminates the lattice mismatch between the substrate and the device layers, thereby reducing the dislocation density of the material. The growth conditions were optimized for material quality and high carrier concentration in the *p*-type region. To minimize the dislocation density of the devices, GaN *p-i-n* diodes were grown on low-dislocation density (~<1×10^{8} cm^{-2}) *n*-type bulk GaN substrates [44]. These device structures and processing steps are identical to the rectifiers grown on SiC substrates. Figures 6.5 and 6.6 illustrate the structure and SEM image of the GaN *p-i-n* rectifier grown on bulk GaN substrate. The forward *I-V* characteristics and low reverse bias voltage (up to –100 V) *I-V* characteristics were measured using an Agilent HP4156C precision semiconductor parameter analyzer. The high-voltage reverse *I-V* characteristics (beyond -100 V) were measured using a high-voltage test system, which consists of a high-voltage power supply (Stanford Research Systems PS350) and a HP 4142B Modular *I-V* analyzer.

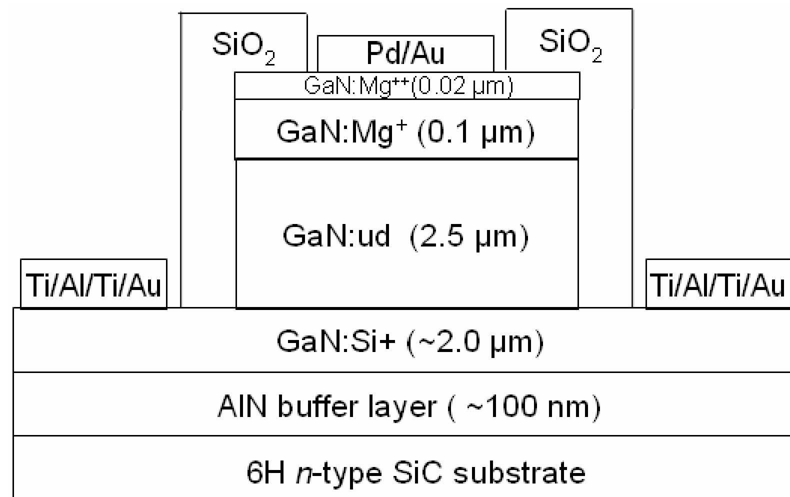

Figure 6.5: A schematic epitaxial layer and device structure.

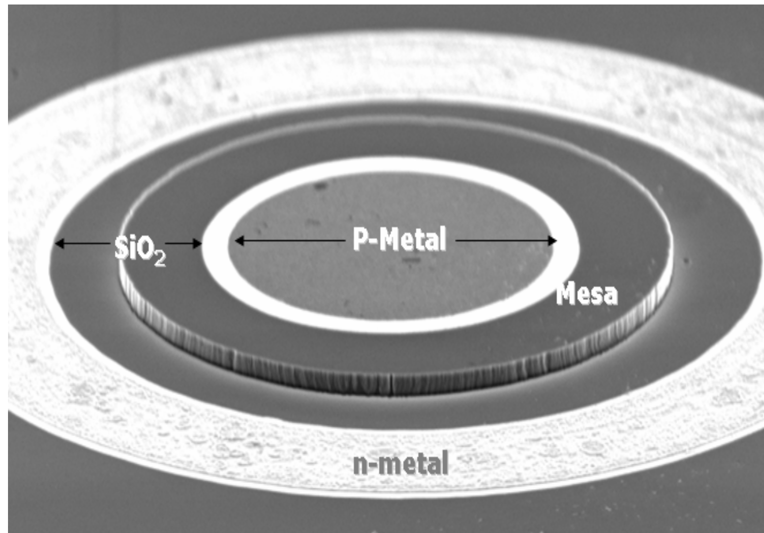

Figure 6.6: SEM image of the *p-i-n* GaN rectifier with a mesa diameter of 80 μm employed in this work.

ICS Metrics software was used to control the hardware [45]. Figure 6.7 shows the high-voltage reverse characteristics obtained from a representative device.

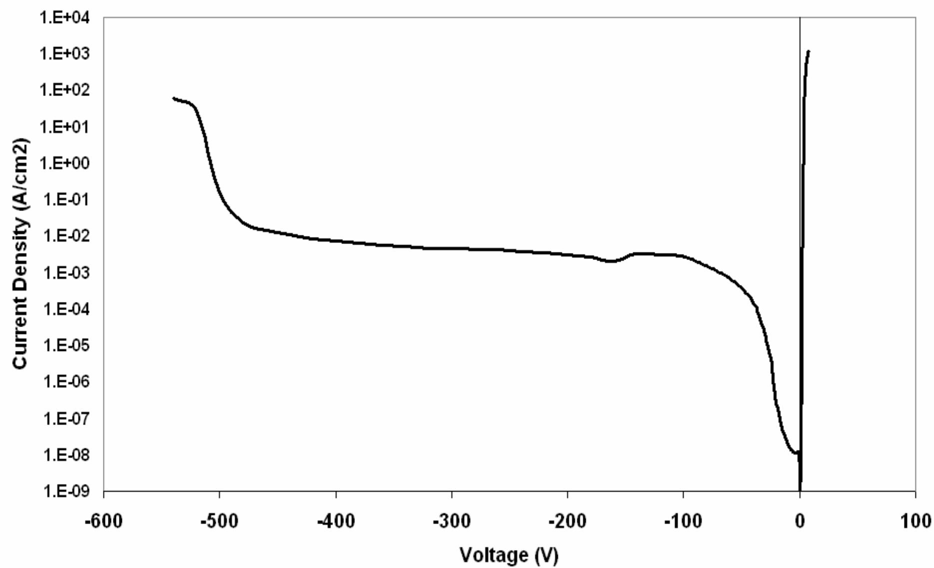

Figure 6.7: Semi-logarithmic plot of the current density versus voltage measured for a typical GaN *p-i-n* rectifier with a mesa diameter of 80 μm.

The reverse current density is ~0.1 A/cm^2 at ~-500 V, with a blocking voltage of ~-540 V. The forward *I-V* characteristics are shown in Figures 6.8 and 6.9. The forward voltage drop is ~4.4 V at a typical forward current density of 100 A/cm^2, with the maximum current density exceeding 1000 A/cm^2. The specific On-resistance is R_{ON} ~3 mΩ·cm^2. These values yield a figure-of-merit value of $(V_{RB})^2/R_{ON}$ = 97.2 MW/cm^2. These values are close to the simulation results for this device structure using a commercial device simulator, which predicts a breakdown voltage of ~-700 V and a forward voltage drop of 3.3 V at a forward current density of 100 A/cm^2 [46]. Analysis of the forward *I-V* characteristics indicate a diode ideality factor of *n*~2.5 at ~2 V, as expected for a recombination dominated transport in the space-charge region. Beyond a forward voltage ~3 V, the current is limited by the device series resistance.

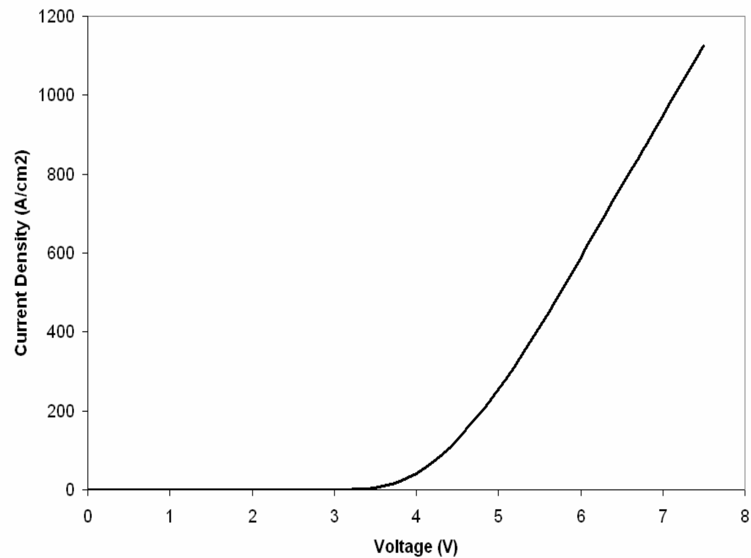

Figure 6.8: Forward *I-V* characteristics for the device with a mesa diameter of 80 µm, in linear-scale.

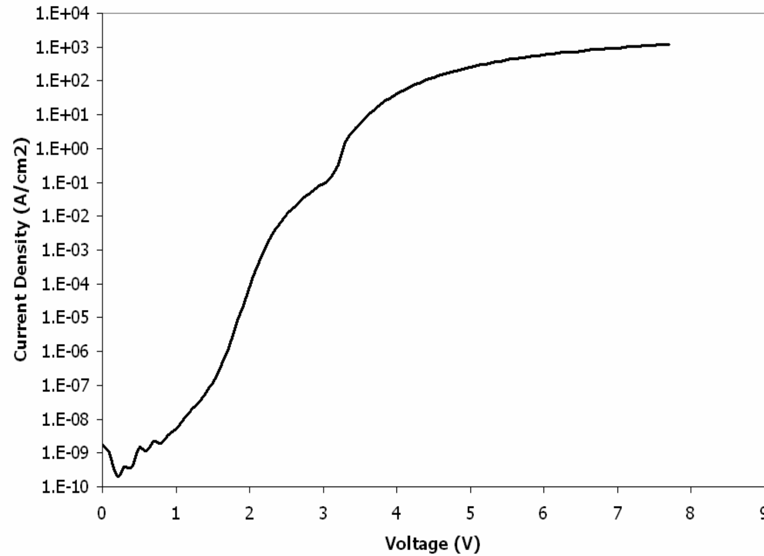

Figure 6.9: Forward *I-V* characteristics for the device with a mesa diameter of 80 μm, in log-scale.

A high forward voltage drop is expected for wide-bandgap materials, especially for direct-bandgap semiconductors like GaN that have extremely short carrier lifetimes relative to indirect-bandgap semiconductors like SiC [47].

6.4 Rectifier Structure on SiC Substrate Using a Conducting Buffer Layer

One of the problems of using AlN as a buffer layer is that it is an insulator, having a large ionization activation energy of ~320 meV for Si donors [48] as well as a large energy bandgap of 6.2 eV. As a result, when a GaN-based device structure is grown on a SiC substrate with an AlN buffer layer, a back-side contact to the SiC substrate with a full-vertical device configuration cannot be realized; hence, with a conventional AlN buffer layer and mesa structure, the excess leakage current through sidewall damage by deep dry etching is unavoidable.

As one of the alternative approaches to avoid the plasma etch, a low Al-composition AlGaN (up to an Al-mole fraction ~0.15), which can be directly grown on SiC substrates with reasonably conductive characteristics, has been investigated. The reason for using AlGaN instead of GaN as a conductive substrate is that the direct growth of GaN on SiC substrates gives low GaN material quality. In this case, GaN three-dimensional islands develop and the surface morphology becomes rough [49]. The best results for GaN/SiC epitaxial structures are usually obtained using AlN, acting as a buffer layer [49].

The growth of GaN *p-i-n* rectifiers on an *n*-type SiC conducting substrate with AlGaN buffer layer enables the structural design of full-vertical rectifiers without using a deep mesa etch, having the *n*-contact on the bottom of the substrate in contrast to the case of insulating substrates. For this approach, however, the phase separation with the fluctuation of Al content and three-dimensional GaN island morphology have been observed [50,51,52,53,54]. The difference in the surface mobility between Al and Ga atoms on the growing surface, which is one of the crucial parameters in AlGaN growth, has also been published [55]. The optimized growth conditions for the AlGaN conducting buffer layer have been used in the device structure. This optimization has been investigated by examining the vertical carrier transport characteristics as well as the surface morphology of the conducting buffer layer.

In this section, the high-voltage performance of GaN *p-i-n* rectifiers employing a full-vertical geometry with $Al_xGa_{1-x}N$:Si ($x = \sim 0.1$) as a conducting buffer layer are demonstrated, with *n*-contacts deposited on the backside of the substrate.

6.4.1 Full-Vertical *p-i-n* Rectifiers

The development of a full-vertical GaN *p-i-n* rectifier on a 6H *n*-type SiC substrate by employing a conducting $Al_xGa_{1-x}N$:Si (x = ~ 0.1) buffer layer scheme is also reported. In this vertical configuration, the *n*-contact is made on the backside of the SiC substrate using a Ni/Au metallization scheme. Epitaxial layers are grown to duplicate the conventional structure with the exception of using a $Al_xGa_{1-x}N$:Si nucleation layer. The conducting $Al_xGa_{1-x}N$:Si layer is seen to provide excellent electrical properties, while also acting as a good nucleation layer for subsequent GaN growth.

To overcome the technological barriers associated with insulating AlN buffer layers, high-temperature grown AlGaN:Si layers were investigated to realize a full-vertical GaN *p-i-n* structure for rectifier applications. The AlGaN:Si layer is required to satisfy two conditions to serve as a conducting buffer layer: (1) It needs to be vertically conducting through the buffer and substrate, and (2) it should be effective as a buffer layer in terms of the crystalline and structural quality for the subsequent growth of epitaxial layers. The AlGaN:Si buffer layer was calibrated to achieve improved crystalline and structural quality by altering growth conditions and epitaxial designs. AlGaN buffer layers were grown on (0001) 6H-SiC *n*-type substrates at a low pressure of 50 Torr to minimize the homogeneous gas-phase reactions between TMAl and NH_3 [56,57], while all of the subsequent GaN layers were grown at 200 Torr. TMAl, TMGa, and NH_3 molar flows were optimized to promote the lateral movement of Al ad-atoms during the growth of AlGaN:Si buffer layers. The Al mole fraction of the AlGaN layer was measured to be approximately 0.1, determined from photoluminescence and XRD. The carrier concentration in the $Al_xGa_{1-x}N$:Si (x= ~ 0.1) layer was estimated to be 3×10^{18}

cm^{-3}. The vertical transport characteristics of n-type $Al_xGa_{1-x}N$:Si (x= ~ 0.1) on an n-type SiC substrate were studied to determine the electrical properties. For this purpose, a metallization scheme using Ti/Al/Ti/Au on top of the n-AlGaN:Si and Ni/Au on the backside of the n-type SiC substrate was deposited by an electron-beam evaporator system. As shown in Figure 6.10, the structure demonstrated good current voltage characteristics between the n-n heterojunction with a 180 μm diameter circular mesa. A small kink was observed on forward-bias condition and it is believed to originate from the heterostructure barrier between n-AlGaN and the n-SiC junction as a result of the band-offset combined with Fermi level pinning effect by the interface defect [58]. Another possibility for the origin of the kink can be non-ideal ohmic contact behavior. However, the ohmic behavior of the contact, especially for n-AlGaN, was verified by transmission line measurement (TLM) study. The surface morphology of the $Al_xGa_{1-x}N$:Si (x= ~ 0.1) conducting buffer layer was also characterized by AFM and it resulted in

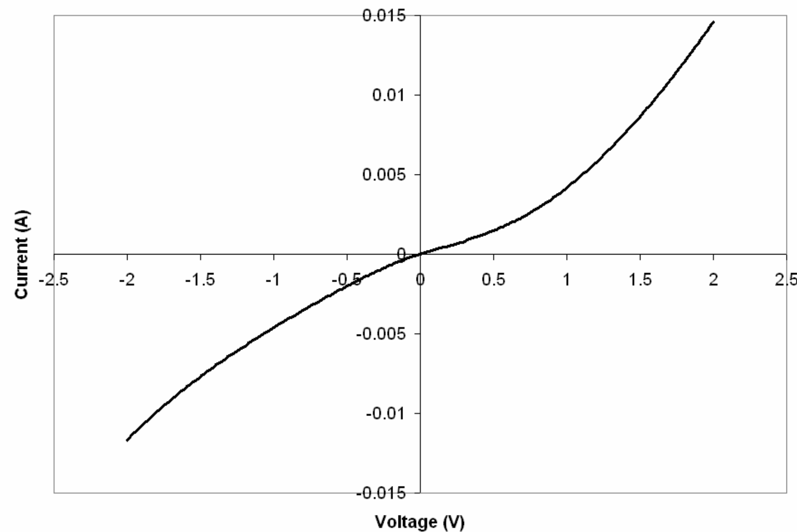

Figure 6.10: The vertical transport characteristics of $Al_{0.1}Ga_{0.9}N$:Si conducting buffer layer grown on an n-type 6H-SiC substrate.

a smooth surface with the RMS roughness values of 0.44 nm and 0.63 nm for a 1×1 μm^2 scan and 5×5 μm^2 scan, respectively.

Examination of the sample surface with a Nomarski optical microscope revealed a smooth surface for a full-vertical GaN *p-i-n* rectifier structure with $Al_xGa_{1-x}N$:Si (x = ~0.1) as a conducting buffer layer. An $Al_xGa_{1-x}N$:Si (x = ~ 0.1) layer graded to a GaN:Si layer was inserted as a strain relaxation layer underneath the *n*-type GaN. The microscopic surface morphology was characterized by AFM. The crystalline quality of GaN epitaxial layers on a conducting buffer layer/SiC substrate for a full-vertical structure was analyzed using a high-resolution X-ray diffractometer. The full-width-at-half-maximum (FWHM) linewidths of the GaN-related peaks were ~227 arc-sec. and ~317 arc-sec. for (002) and (102) scan, respectively, which are comparable to those of GaN *p-i-n* rectifier structures employing a conventional AlN buffer layer on SiC substrates.

The epitaxial structure for a full-vertical rectifier is similar to that of the vertical mesa device. It consists of, from top to bottom layers, GaN:Mg^{++} contact layer, *p*-GaN:Mg, 2.5 μm-thick unintentionally doped GaN, *n*-GaN:Si, and AlGaN:Si conducting buffer layer. The schematic structure of a full-vertical GaN *p-i-n* rectifier is illustrated in Figure 6.11 (a). The energy band diagram of the epitaxial structure for the device is also shown in Figure 6.11 (b). For the construction of the energy band diagram, one-dimensional simulation [59] was applied to the GaN *p-i-n* structure. The intrinsic doping level of unintentionally doped *i*-GaN was assumed to be n~5×10^{16} cm^{-3}, and the spontaneous and piezoelectric polarization effect was not considered in the simulation.

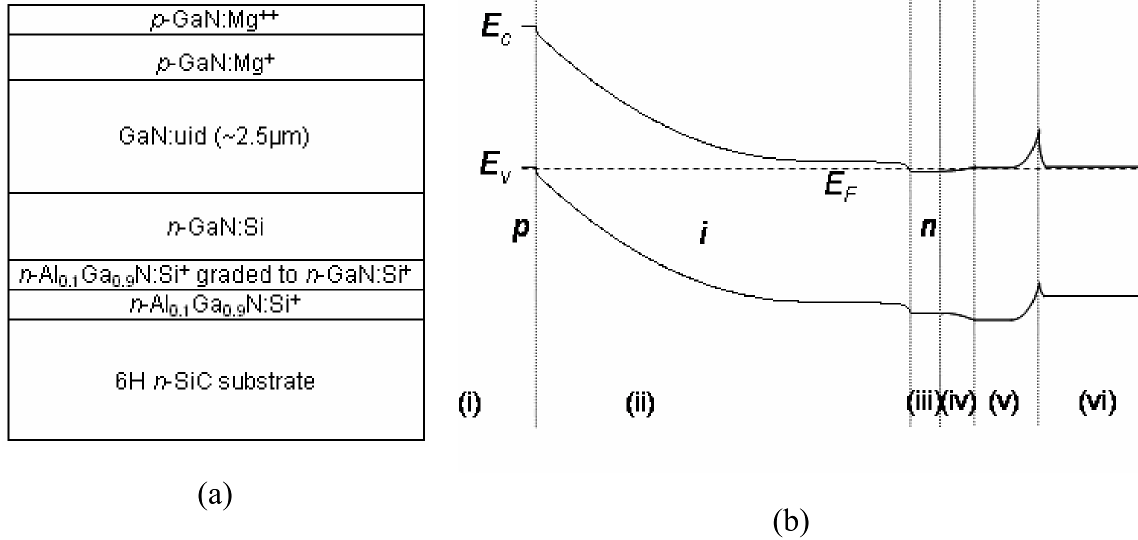

Figure 6.11: (a) Schematic structure of a full-vertical GaN *p-i-n* rectifier used in this work and (b) energy band diagram of the epitaxial structure in thermal equilibrium: (i) *p*-GaN:Mg, (ii) unintentionally doped *i*-GaN, (iii) *n*-GaN:Si, (iv) AlGaN-GaN grading, (v) AlGaN conducting buffer layer , and (vi) *n*-SiC substrate.

The top *p*-type contact was a circular pattern, while the *n*-type contact covered most of the backside of the SiC substrate. Two configurations of devices were compared: One does not have any current guiding scheme, and the other has current guiding only in the *p*-layer. A comparison of the two structures is shown in Figures 6.12 (a) and 6.12 (b).

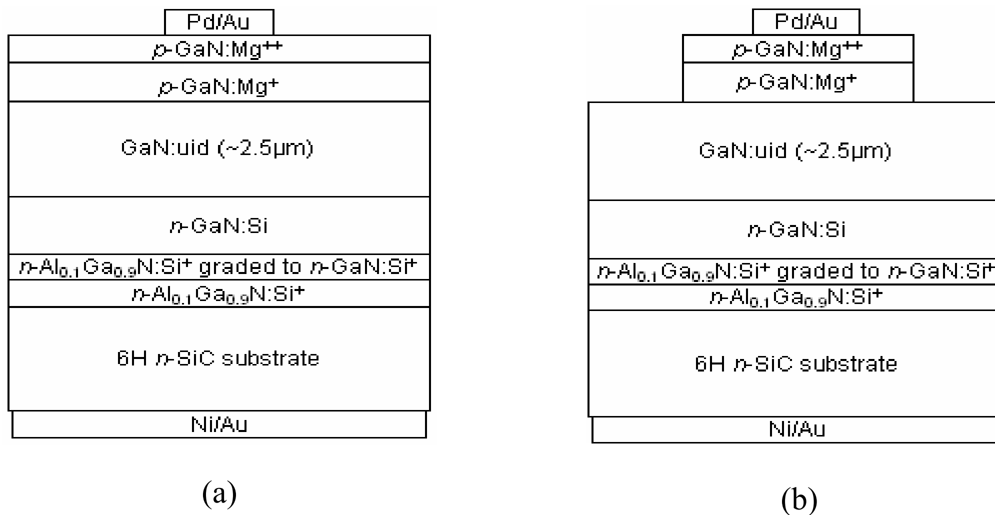

Figure 6.12: A full-vertical GaN *p-i-n* rectifier (a) without a current guiding isolation in the *p*-layer. (b) with a current guiding isolation in the *p*-layer.

To provide the current guiding in the *p*-layer, the layer was shallow etched by ICP etching and passivated by SiO_2. Performance characteristics were compared. Both configurations showed a low on-resistance of 7.5×10^{-3} m$\Omega \cdot$cm^2. The reverse breakdown voltage for rectifiers without *p*-current guiding was over -330 V [60], while one with *p*-current guiding was over -400 V (Figure 6.13). The devices with a *p*-current guiding exhibited a much reduced reverse leakage current, indicating that the current guiding (even in the relatively thin *p*-layer) facilitated the reduction of the reverse leakage current and improved the device performance characteristics.

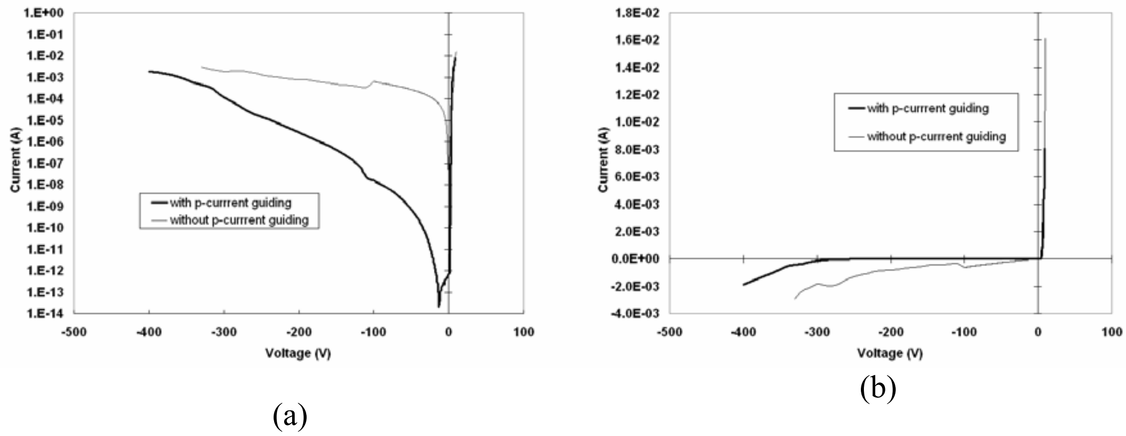

(a) (b)

Figure 6.13: (a) Current-voltage characteristics of a full-vertical GaN *p-i-n* rectifier (log-scale) (b) Current-voltage characteristics of a full-vertical *p-i-n* rectifier (linear scale).

6.5 Summary

The goal of this chapter was to develop high-voltage III-nitride *p-i-n* rectifiers with low on-resistances. We have grown, fabricated and characterized *p-i-n* rectifiers using the vertical-mesa technology as well as the full-vertical method. Although full-vertical rectifiers avoid the deep-etching of the sidewalls, the highest figure-of-merit value devices were fabricated on the vertical-mesa devices. For mesa rectifiers grown on 6H-SiC substrates, a power figure-of-merit value of $(V_{RB})^2/R_{ON}$ = 108 MW/cm^2 was achieved. To our knowledge, this figure-of-merit value is the best reported for vertical mesa GaN *p-i-n* rectifiers with comparable *i*-layer thicknesses.

CHAPTER 7

RESEARCH SUMMARY AND FUTURE WORK

7.1 Avalanche Photodiodes

The development of very high gain III-nitride APDs have been described in this work. An optical gain of over 3000 has been obtained for GaN APDs for the first time. Also, AlGaN APDs with true avalanche gain has been obtained as well. These results suggest that although the gains achieved for GaN based detectors are high enough for possible Gieger-mode operations, there is still room for major breakthrough in $Al_xGa_{1-x}N$ based APDs. Major breakthrough has to be made especially in the growth part of AlGaN based materials. With the recent commercial availability of AlN substrates, it may be possible to expand new research efforts to the development of solar-blind AlGaN avalanche photodiodes since AlN is a better lattice-matched substrate for the growth of $Al_xGa_{1-x}N$, for $x > 0.5$.

Towards the goal of achieving AlGaN APDs with $x > 0.5$, we have optimized the *n*-contact TLM characteristics for *n*-type $Al_{0.52}Ga_{0.48}N$. By using vanadium (V) instead of titanium (Ti) as the first metal layer for deposition, specific contact resistivity values as low as $4.15\times10^{-5}\ \Omega\cdot cm^2$ was achieved. This is a significant improvement over Ti based contacts, with contact resistivity values of $\sim2\times10^{-3}\ \Omega\cdot cm^2$. The TLM characteristics of the *n*-type contacts are shown in Figure 7.1. Such a result suggests that for AlGaN APDs with high Aluminum compositions, Vanadium could be a more suitable *n*-contact metal.

Although some preliminary experimental work was performed, growth conditions would need to be further optimized for AlGaN APDs with $x > 0.5$. Also, III-Nitride APDs with Gieger-mode operations need to be demonstrated as future work.

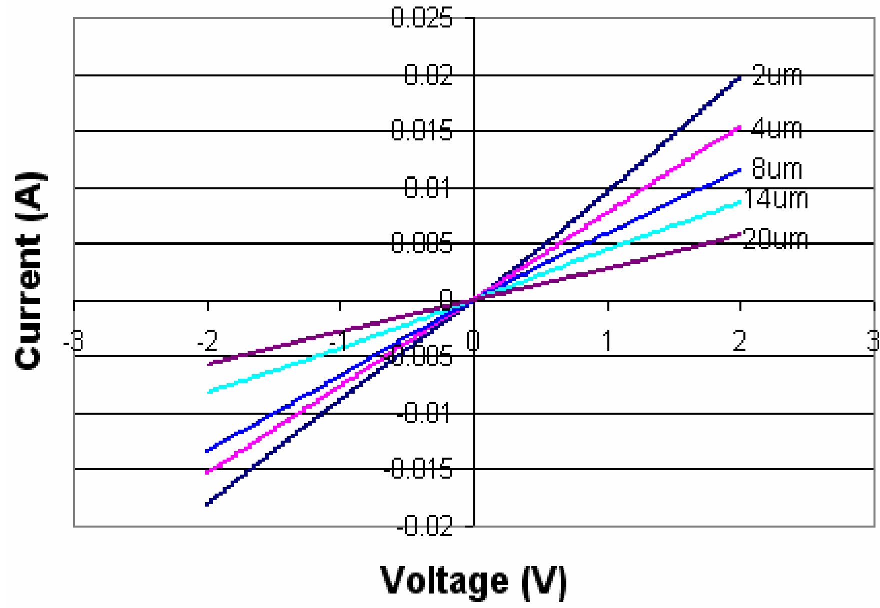

Figure 7.1: Vanadium/Aluminum/Titanium/Gold *n*-contact *I-V* characteristics of an *n*-type $A_{0.52}G_{0.48}aN$ layer with different contact spacings. Specific contact resistivity was measured and calculated to be 4.15×10^{-5} $\Omega\cdot cm^2$. Metal was annealed at 750 ^oC in Nitrogen ambient.

7.2 Green Light Emitting Diodes

The development of Group III-Nitride has played a major role in the high-brightness LEDs. While much success has been reported in the development of LEDs in the blue and violet spectral region, less success has been demonstrated in obtaining high quantum efficiencies and low forward voltages for LEDs operating in the green and longer wavelength regime (~545 nm). In this work, we have used an active region friendly *p*-type InGaN to reduce the degradation of the active region, which contains a high composition of Indium (> 20%). First, we have compared the effects of InGaN:Mg and GaN:Mg on the electrical and optical properties of the LEDs. We have shown that by employing InGaN:Mg as the *p*-layer, the emission light intensity of the diode increases, and the series resistance of the diode decreases. By employing InGaN:Mg as the *p*-layer, we have grown, fabricated and characterized LEDs operating in the green (526 nm) and longer wavelengths (545 nm). The peak internal quantum efficiencies were extracted to be 25% and 13% respectively, for these samples. For LEDs emitting at ~526 nm, a forward voltage of 3.66 V at 20 mA and a diode series resistance of 17.3 Ω was achieved, for device dimensions of 350 × 350 μm^2. For LEDs emitting at ~545 nm at 20 mA of drive current, a forward voltage of 3.58 V was achieved for device dimensions of 350 μm by 350 μm, with a diode series resistance of only 16.5 Ω. However, for these structures, there was an abrupt heterojunction between the *p*-InGaN and the GaN QWB layer underneath.

As part of the future work, we would like to first propose the use of a compositional grading from InGaN in the *p*-layer to the GaN QW barrier below, to minimize the barrier due to this abrupt heterojunction. Secondly, we like to modify the

structure of the LEDs to improve the efficiency. To improve the brightness, we can increase the thicknesses of the *n*- and *p*-layers to enhance the carrier spreading before carrier recombination in the active region. Thirdly, we can investigate the reliability of the green LEDs employing the *p*-InGaN layers. The LEDs with *p*-InGaN layers have a higher density of v-defects compared to LEDs with *p*-GaN layers. To test the reliability of the diodes employing *p*-InGaN layers, the lifetime of the LEDs should be measured. Also, the leakage current of the diodes should be investigated under reverse-bias conditions. If the leakage current is too high compared to LEDs employing *p*-GaN layers, then growth conditions will need to be optimized to reduce the v-defects, which exist in *p*-InGaN layers. The reduction of defect densities should also increase the lifetime of the diodes.

Towards the goal of reducing the density of v-defects as well as achieving low leakage devices for LEDs with *p*-InGaN based materials, a *p*-type layer utilizing super-lattice (SL) structure is proposed. By employing such a structure, the reverse leakage characteristics for the LEDs were reduced. A comparison of LEDs with different *p*-layers is shown in Figure 7.2. Clearly, an LED employing *p*-InGaN super-lattice showed a reduced reverse leakage current compared to an LED with *p*-InGaN. Also, the *p*-TLM of the LED with *p*-SL showed higher conductivity values compared to the *p*-TLM characteristics of an LED with *p*-InGaN. This is shown in Figure 7.3. The Indium composition is measured to be 4% for both *p*-InGaN and *p*-SL.

Although a reduction in leakage current as well as an improvement in *p*-layer conductivity was demonstrated by the use of a *p*-SL, further optimizations in device

structures and growth conditions will be necessary for improvement of LEDs emitting in the green and longer wavelengths (540nm~580nm).

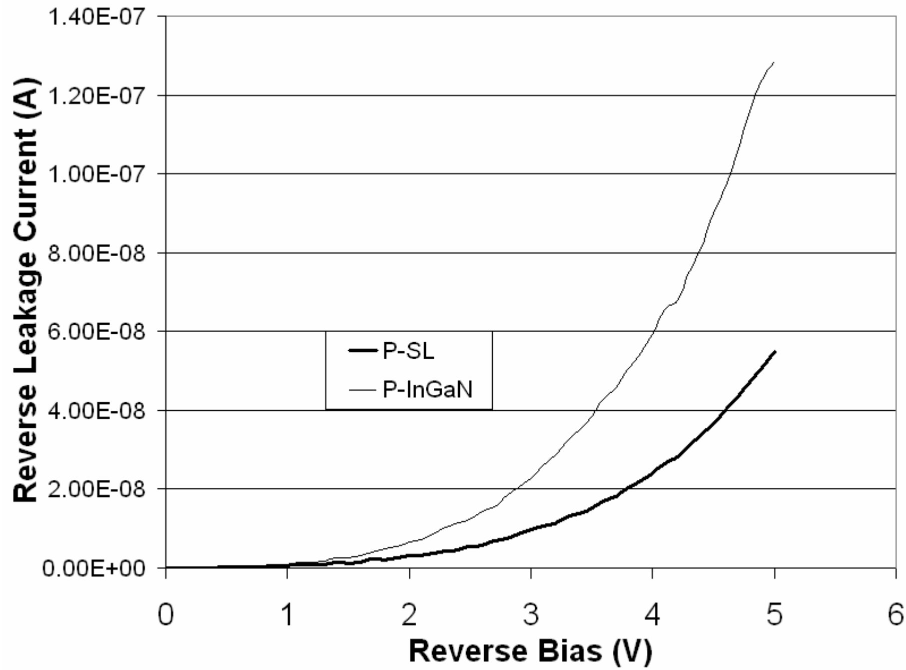

Figure 7.2: Comparison of reverse leakage *I-V* characteristics between an LED employing *p*-InGaN super-lattice, and an LED with a *p*-InGaN layer.

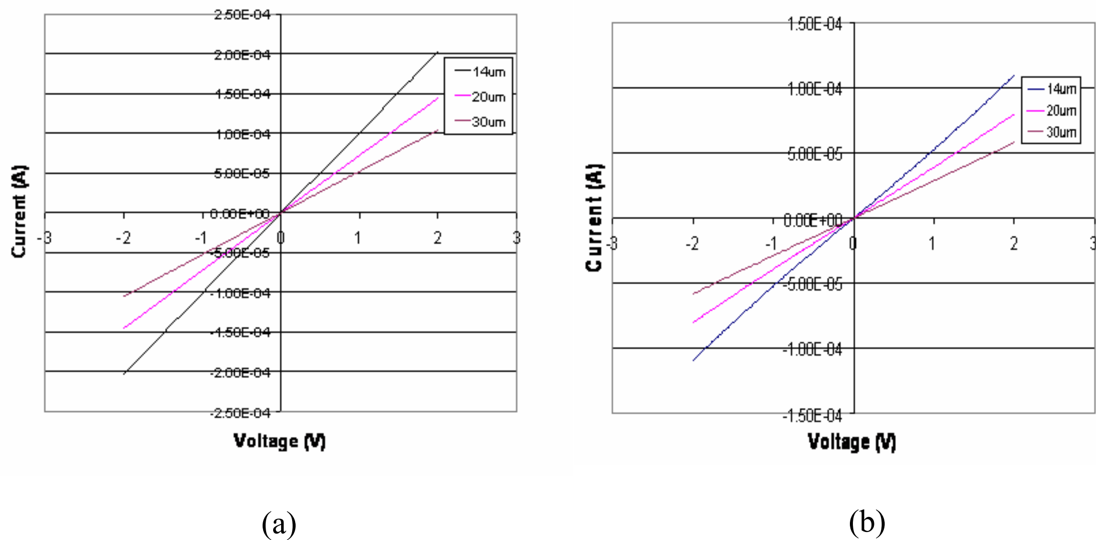

Figure 7.3: Transparent Ni/Au *p*-contact characteristics of Green LEDs with different *p*-layers: (a) *p*-TLM on LED with *p*-InGaN super-lattice (b) *p*-TLM on LED with *p*-InGaN layer.

7.3 PIN Rectifiers

GaN *p-i-n* rectifiers grown on SiC and GaN substrates have been investigated in this report. First, a study was undertaken on rectifiers using the conventional mesa structure. Devices were grown on both 6H-SiC substrate and GaN substrate. Both devices exhibited breakdown voltages greater than 500 V, and on-resistances less than 3 $m\Omega \cdot cm^2$. However, diode ideality factors greater than 2 have been measured. The higher than expected ideality factors may have been contributed from the mesa sidewalls. To investigate the effects due to sidewalls, current density measurements and ideality factor calculations on larger area devices are proposed as future work. By comparing the current densities for different mesa size devices, the contribution of current from the sidewall or bulk can be analyzed.

For these mesa structures, however, the excess leakage current through sidewall damage by deep dry etching is unavoidable. Also, metal contacts on the etched surface can cause field crowding near the bottom of the sidewalls. As an alternative approach, we have also investigated the full-vertical rectifier structure, by depositing *n*-contacts on the backside of the substrate. This approach avoids the deep dry etching as well as the field crowding of the conventional mesa structure. For this approach, both the substrate and the buffer layer have to be conductive. With an optimized conductive AlGaN buffer layer, the design, fabrication and characterization of full-vertical rectifiers were report as the last part of chapter 6.

REFERENCES

1. UV-enhanced PMTs are typically based upon Cs-Te photocathodes such as that used in the Hamamatsu R1080 PMT; Hamamatsu Photonics, K. K. <http://usa.hamamatsu.com/>. Website was accessed on February 2006.

2. T. Isoshima, Y. Isojima, K. Hakomori, K. Kikuchi, K. Nagai, and H. Nakagawa, "Ultrahigh sensitivity single-photon detector using a Si avalanche potodiode for the measurement of ultraweak biochemiluminescence," *Rev, Sci, Instrum*. 66, 2922 (1995).

3. J. L. Pau, E. Monroy, M. A. Sanchez-Garcia, E. Calleja, and E. Munoz, "AlGaN ultraviolet photodetectors grown by molecular beam epitaxy on Si(111) substrates," *Mater. Sci, Eng., B* 93. 159 (2002).

4. C. J. Collins, U. Chowdhury, M. M. Wong, B. Yang, A. L. Beck, R. D. Dupuis and J. C. Campbell, "Improved solar-blind detectivity using an AlGaN heterojunction *p*-*i*-*n* photodiode," *App. Phys. Lett*., 80, 1770 (2002).

5. P. Lamarre, A. Hairston, S. P. Tobin, K. K. Wong, A. K. Sood, M. B. Reine, M. Pophristic, R. Birkman, I. T. Ferguson, R. Singh, C. R. Eddy, Jr. , U. Chowdhury, M. M. Wong, R. D. Dupuis, P. Kozodoy and E. J. Tarsa, "AlGaN UV Focal Plane Arrays," *Physica Status Solidi A*, 188, 289 (2001).

6. S. Muthu, F. J. P. Schuurmans, and M. D. Pashley, "Red, green, and blue LEDs for white light illumination," *IEEE J. Select. Topic Quantum Electron*. 8, 333 (2002).

7. M. Krames, 2003 DOE Solid State Lighting Program Planning Workshop, November 13-14, Washington, D.C. (2003).

8. K. J. Schoen, J. M. Woodall, J. A. Cooper, and M.R. Melloch, "Design Considerations and Experimental Analysis of High Voltage SiC Schottky Barrier Rectifiers," *IEEE Trans. Electron. Dev*, 45, 1595 (1998).

9. M. Trivedi, and K. Shenai, "Performance Evaluation of High-Power Wide Band-Gap Semiconductor Rectifiers," *J. Appl. Phys*., 85, 6889 (1999).

10. C. J. Eiting, Doctoral Dissertation, The University of Texas at Austin (1999).

11. D. C. Joy, A. D. Romig, Jr., and J. I. Goldstein, Principles of Analytical Electron Microscopy, Plenum, New York, 1986.

12. D. Sarid, *Scanning Force Microscopy with Applications to Electric, Magnetic, and Atomic Forces*, Oxford University Press, Oxford, (1991).

13. P. Bhattacharya, Semiconductor Optoelectronic Devices, Prentice Hall, NJ, 1997.

14. B. G. Streetman, Solid State Electronic Devices, Prentice Hall, NJ, 1990.

15. K. Gillessen, and W. Schairer, Light Emitting Diodes-An Introduction. Prentice Hall, NJ, 1987

16. H. Kressel, and J. K. Butler, Semiconductor Lasers and Heterojunction LEDs, Academic Press, New York, 1977.

17. S. K. Ghandhi, Semiconductor Power Devices, Wiley, New York 1997.

18. S.C. Choo, "Effect of carrier lifetime on the forward characteristics of high-power devices," *IEEE Trans. Electron Devices*, **17**, 647 (1970).

19. X. Xin, F. Yan, X. Sun, P. Alexandrove, C. M. Stahle, J. Hu, M. Matsumara, X. Li, M. Weiner and H. J. Zhao, "Demonstration of 4H-SiC UV single photon counting avalanche photodiodes," *Electron. Lett*., 41, 1192 (2005).

20. X. Guo, L. B. Rowland, G. T. Dunne, J. A. Fronheiser, P. M. Sandvik, A. L. Beck, and J. C. Campbell, "Demonstration of Ultraviolet Separate Absorption and Multiplication 4H-SiC Avalanche Photodiodes," *IEEE photonics tech. Lett.,* 18, 136 (2006).

21. K. Burr, P. Sandvik, S. Arthur, D. Brown, and K. Matocha, "Fabrication and Measurement of 4H-Silicon Carbide Avalanche Photodiodes," *Mat. Res. Soc. Symp. Proc.* Vol. 742, Paper K7.8.1 (2003).

22. K. A. McIntosh, R. J. Molnar, L. J. Mahoney, K. M. Molvar, N. Efremow, Jr., and S. Verghese, "Ultraviolet photon counting with GaN avalanche photodiodes," *Appl. Phys. Lett.* 75, 3485 (1999).

23. B. Yang, T. Li, K. Heng, C. J. Collins, S. Wang, A. Beck, R. D. Dupuis, and J. C. Campbell, "Low Dark Current GaN Avalanche Photodiodes," *Appl. Phys. Lett*. 76, 924 (2000).

24. S. Verghese, K. A. McIntosh, R. J. Molnar, L. J. Mahoney, R. L. Aggarwal, M. W. Geis, K. M. Molvar, E. K. Duerr, and I. Melngailis, "GaN Avalanche Photodiodes Operating in Linear-Gain Mode and Geiger Mode," *IEEE Trans. Electron Devices* 48, 502 (2001).

25. J. C. Carrano, D. J. H. Lambert, C. J. Eiting, C. J. Collins, T. Li, S. Wang, B. Yang, A. L. Beck, R. D. Dupuis, and J. C. Campbell, "GaN avalanche photodiodes," *Appl. Phys. Lett.* 76, 924 (2000).

26. Reference 20 reported avalanche gain as high as *M*~300 limited by saturation of the lock-in amplifier.

27. The substrates were provided by Kyma Technologies, Inc.

28. The system was manufactured by Thomas Swan Scientific Equipment, Ltd., Cambridge UK.

29. Obtained from Epichem Inc., Haverhill, MA.

30. J. B. Limb, D. Yoo, J. H. Ryou, W. Lee, S. C. Shen, R. D. Dupuis, M. L. Reed, C. J. Collins, M. Wraback, D. Hanser, E. Preble, N. M. Williams, and K. Evans, "GaN Ultraviolet Avalanche Photodiodes with Optical Gain Greater than 1,000 Grown on GaN Substrates by Metalorganic Chemical Vapor Deposition," *Appl. Phys. Lett.* 89, 011112 (2006).

31. M. Krames, 2003 DOE Solid State Lighting Program Planning Workshop, November 13-14, Washington, D.C. (2003).

32. F. A. Ponce, S. Srinivasan, A. Bell, L. Geng, R. Liu, M. Stevens, J. Cai, H. Omiya, H. Marui, and S. Tanaka**, "**Microstructure and electronic properties of InGaN alloys," *Phys. Stat. Sol. B* 240, 273 (2003).

33. A. Hangleiter, J. S. Im, H. Colmer, S. Heppel, J. Off, S. Scholz, "The role of piezoelectric fields in GaN-based quantum wells," *MRS Internet J. Nitride Semicond. Res.* **3**, 15 (1998).

34. K. Kumakura, T. Makimoto, N. Kobayashi, "Mg-acceptor activation mechanism and transport characteristics in *p*-type InGaN grown by metalorganic vapor phase epitaxy, " *J. Appl. Phys***.** 93, 3370 (2003).

35. Manufactured by Thomas Swan Scientific Equipment.

36. Wonseok Lee, Jae Limb, Jae-Hyun Ryou, Dongwon Yoo, Theodore Chung, and Russell Dupuis, "Effect of thermal annealing induced by *p*-type layer growth on blue and green LED performance," *J. Crystal Growth* 287, 577 (2006).

37. Wonseok Lee, Jae Limb, Jae-Hyun Ryou, Dongwon Yoo, Theodore Chung, and Russell Dupuis, "Influence of growth temperature and growth rate of *p*-GaN layers on the characteristics of green light emitting diodes," *J. Electron. Mater*. 35, 587 (2006).

38. X. H. Wu, C. R. Elsass, A. Abare, M. Mack, S. Keller, P. M. Petroff, S. P. Denbaars, and J. S. Speck, **"**Structural origin of V-defects and correlation with localized

excitonic centers in InGaN/GaN multiple quantum wells," Appl. Phys. Lett. **72** 692 (1998).

39. J. B. Limb, W. Lee, J. H. Ryou, D. Yoo, and R. D. Dupuis, "Comparison of GaN and $In_{0.04}Ga_{0.96}N$ *p*-layers on the electrical and electroluminescence properties of green light emitting diodes," *J. Electron. Mater*. 36, 426 (2007)

40. Ting Gang Zhu, Doctoral Dissertation, The University of Texas at Austin (2003).

41. J. Zolper, M.Skowronski, "Advances in Silicon Carbide Electronics," *MRS Bulletin* 30, 273 (2005).

42. T. Weeks Jr., M. Bremser, K. Ailey, E. Carlson, W. Perry, and R. Davis, **"**GaN thin films deposited via organometallic vapor phase epitaxy on α(6H)–SiC(0001) using high-temperature monocrystalline AlN buffer layers," *Appl. Phys. Lett*. 67, 401 (1995).

43. J. B. Limb, D. Yoo, J.-H. Ryou, S.-C. Shen, and R. D. Dupuis, "Low on-Resistance GaN PIN rectifiers grown on 6H-SiC substrates," ***Electron. Lett***. 43, p. 366-367 (2007).

44. The substrates were estimated to have a dislocation density of $\sim 10^{7}$ cm^{-2}.

45. J. B. Limb, D. Yoo, J.-H. Ryou, W. Lee, S.-C. Shen, and R.D. Dupuis, "High performance GaN PIN rectifiers grown on free standing GaN substrates," *Electron. Lett*. 42 1313 (2006).

46. B.S. Shelton, T.G. Zhu, D.J.H. Lambert,., and R.D. Dupuis, 'Simulation of the Electrical Characteristics of High-Voltage Mesa and Planar GaN Schottky and PIN Rectifier', *IEEE Trans. Electron. Dev.*, 2001, 45, pp. 1498-1502

47. L. Chernyak, A. Osinsky, H. Temkin, J.W. Yang, O. Chen, and M. A. Khan, 'Electron Beam Induced Current Measurements of Minority Carrier Diffusion Length in Gallium Nitride', *Appl. Phys. Lett.,* 1996, 69, pp.2531-2533

48. R. Zeisel, M. W. Bayerl, S. T. B. Goennenwein, R. Dimitrov, O. Ambacher, M. S. Brandt, and M. Stutzmann, *Phys. Rev. B* 61, R16283 (2000).

49. W. G. Perry, T. Zheleva, M. D. Bremser, R. F. Davis, W. Shan, and J. J. Song, "Correlation of Biaxial Strains, Bound Exciton Energies, and Defect Microstructures in GaN Films Grown on AlN/6H-SiC(001) Substrates," *J. Electron. Mater*., 26, 224 (1997).

50. H. Lahréche, P. Vennégués, M. Vaille, B. Beaumont, M. Laügt, P. Lorenzini, and P. Gibart, “Comparative study of GaN layers grown on insulating AlN and conductive AlGaN buffer layers,” *Semicond. Sci. Technol*. 14, L33 (1999).

51. P. Vennéguès and H. Lahrèche, “Phase separation in metalorganic vapor-phase epitaxy $Al_xGa_{(1-x)}N$ films deposited on 6H–SiC,” *Appl. Phys. Lett*. 77, 4310 (2000).

52. B. Moran, M. Hansen, M. Craven, J. Speck, and S. DenBaars, "Growth and characterization of graded AlGaN conducting buffer layers on n+ SiC substrates," *J. Crystal Growth* 221, 301 (2000).

53. R. Kröger, S. Einfeldt, R. Chierchia, D. Hommel, Z. Reitmeier, R. Davis, and Q. Liu, “On the microstructure of $Al_xGa_{1-x}N$ layers grown on 6H-SiC(0001) substrates,” *J. Appl. Phys*. 97, 083501 (2005).

54. A. Petersson, A. Gustafsson, L. Samuelson, S. Tanaka, and Y. Aoyagi, “Compositional variation of AlGaN epitaxial films on 6H-SiC substrates determined by cathodoluminescence,” *MRS Internet J. Nitride Semicond. Res*. 7, 5 (2002).

55. S. Heikman, S. Keller, S. DenBaars, U. Mishra, F. Bertram, and J. Christen, "Non-planar selective area growth and characterization of GaN and AlGaN," *Jpn. J. Appl. Phys.,* 42, 6276 (2003).

56. C. Chen, H. Liu, D. Steigerwald, W. Imler, C. Kuo, and M. Craford, “A Study of Parasitic Reactions Between NH3 and TMGa or TMAl,” *J. Electron. Mater*., 25, 1004 (1996).

57. J. Han, J. Figiel, M. Crawford, M. Banas, M. Bartram, R. Biefeld, Y. K. Song, and A. Nurmikko, “OMVPE growth and gas-phase reactions of AlGaN for UV emitters, ” *J. Crystal Growth* 195, 291 (1998).

58. Y. Huang, X. D. Chen, S. Fung,C. D. Beling, C. C. Ling, X. Q. Dai, and M. H. Xie, “Current transport property of *n*-GaN/*n*-6H–SiC heterojunction: Influence of interface states,” *Appl. Phys. Lett*. 86, 122102 (2005).

59. 1-D Poisson by Prof. Gregory Snider with the University of Notre Dame was used.

60. D. Yoo, J. Limb, J.-H. Ryou, W. Lee, and R. D. Dupuis, “GaN Full-Vertical *p-i-n* Rectifiers Employing AlGaN:Si Conducting Buffer Layers on n-SiC Substrates,” *Appl. Phys. Lett.* 88, 193503 (2006).

VITA

Jae Boum Limb was born in Seoul, South Korea. He received his B.S. degree in Radio Communication Engineering from Yonsei University, South Korea. He also received his M.S. degree in Electrical and Computer Engineering from University of California at Santa Barbara. Currently, he is working towards his Ph.D. degree in Electrical and Computer Engineering at Georgia Institute of Technology, under the supervision of Professor Russell Dean Dupuis. His research interests include III-Nitride based electronic and optoelectronic devices. He has authored/coauthored over 20 technical journal papers and 25 conference presentations, in the field of semiconductor devices and materials.